The Astrophysical Journal, 857:46 (21pp), 2018 April 10 https://doi.org/10.3847/1538-4357/aab3de

The Initial Mass Function of the First Stars Inferred from Extremely Metal-poor Stars

Miho N. Ishigaki[1], Nozomu Tominaga[1,2], Chiaki Kobayashi[1,3], and Ken'ichi Nomoto[1]
[1] Kavli Institute for the Physics and Mathematics of the Universe (WPI), The University of Tokyo, Kashiwa, Chiba 277-8583, Japan; miho.ishigaki@ipmu.jp
[2] Department of Physics, Faculty of Science and Engineering, Konan University, 8-9-1 Okamoto, Kobe, Hyogo 658-8501, Japan
[3] School of Physics, Astronomy and Mathematics, Centre for Astrophysics Research, University of Hertfordshire, College Lane, Hatfield AL10 9AB, UK
Received 2017 October 26; revised 2018 February 19; accepted 2018 February 23; published 2018 April 11

Abstract

We compare the elemental abundance patterns of ∼200 extremely metal-poor (EMP; [Fe/H] < -3) stars to the supernova yields of metal-free stars, in order to obtain insights into the characteristic masses of the first (Population III or Pop III) stars in the universe. The supernova yields are prepared with nucleosynthesis calculations of metal-free stars with various initial masses ($M = 13$, 15, 25, 40 and $100\,M_{\odot}$) and explosion energies ($E_{51} = E/10^{51}$[erg] = 0.5–60), to include low-energy, normal-energy, and high-energy explosions. We adopt the mixing-fallback model, to take into account possible asymmetry in the supernova explosions, and the yields that best fit the observed abundance patterns of the EMP stars are searched by varying the model parameters. We find that the abundance patterns of the EMP stars are predominantly best-fitted by the supernova yields with initial masses $M < 40\,M_{\odot}$, and that more than than half of the stars are best-fitted by the $M = 25\,M_{\odot}$ hypernova ($E_{51} = 10$) models. The results also indicate that the majority of the primordial supernovae have ejected 10^{-2}–$10^{-1}\,M_{\odot}$ of ^{56}Ni, leaving behind a compact remnant (either a neutron star or a black hole), with a mass in the range of ∼1.5–5 $M_{\odot}$. These results suggest that the masses of the first stars responsible for the first metal enrichment are predominantly $<40\,M_{\odot}$. This implies that the higher-mass first stars were either less abundant, directly collapsed into a black hole without ejecting heavy elements, or a supernova explosion of a higher-mass first star inhibits the formation of the next generation of low-mass stars at [Fe/H] < -3.

Key words: stars: abundances – stars: Population III – supernovae: general

Supporting material: machine-readable table

1. Introduction

The nature of the first (Population III or Pop III) stars is crucial in constraining the environment of stars and galaxy formation in the early universe. The most important characteristics of the Pop III stars are their typical masses and the initial mass function (IMF). The masses of the Pop III stars determine the amount of ionizing photons emitted during stellar evolution, and thus they are important to better quantify the contribution of Pop III stars to the cosmic reionization (e.g., Tumlinson et al. 2004). Furthermore, the Pop III stars are responsible for the first metal enrichment in the universe, which is one of the important condition for the formation of the first low-mass stars (Bromm & Loeb 2003; Omukai et al. 2005). Thus, the amount and composition of elements synthesized and ejected by the Pop III stars have a significant impact on the subsequent formation of stars and galaxies (e.g., Bromm & Yoshida 2011; Karlsson et al. 2013).

Previous theoretical studies on the formation of the Pop III stars, based on cosmological simulations, suggest that the Pop III stars were predominantly very massive, with a characteristic mass exceeding $\sim 100\,M_{\odot}$ (e.g., Bromm & Larson 2004, and references therein). Recent high-resolution simulations taking into account more detailed physical processes, however, predict that less-massive stars with a few tens of $M_{\odot}$ can form, and that the mass ranges extend from subsolar to thousands of $M_{\odot}$ (Clark et al. 2011; Greif et al. 2011; Hosokawa et al. 2011, 2016; Stacy & Bromm 2013; Susa 2013; Hirano et al. 2014; Susa et al. 2014; Stacy et al. 2016). The various mass ranges predicted by the simulations could partly depend on details of the simulation techniques and/or numerical resolutions, and thus a clear consensus on the characteristic mass has not been established yet.

Currently, it is not practically feasible to directly observe the Pop III stars, which are believed to be formed at redshifts of 20–30. Thus, the most important observational probes of the masses of the Pop III stars are elemental abundance patterns in long-lived stars: the so-called "extremely metal-poor" (EMP; [Fe/H] < -3) stars. Pop III stars are initially formed out of primordial (i.e., H and He) gas, and produce heavy elements according to their masses and supernova explosion energies. The elements are ejected to the interstellar medium via supernovae, whose elemental yields depend on mixing and fallback within the progenitor Pop III SNe (Umeda & Nomoto 2002; Zhang et al. 2008). The ejecta from the supernova sweep up hydrogen in the interstellar medium with a certain degree of anisotropy, which determines the abundances (e.g., [Fe/H]) in the next-generation stars (Audouze & Silk 1995; Greif et al. 2007; Ritter et al. 2012; Sluder et al. 2016). These diluted ejecta may cool and fragment, from which low-mass stars can form, if the energy injection by the Pop III SNe has not destroyed the host dark matter halo (Kitayama & Yoshida 2005; Cen & Riquelme 2008; Whalen et al. 2008; Smith et al. 2015; Ritter et al. 2016; Chen et al. 2017b).

Given the potentially complex nature of the heavy-element enrichments by the Pop III SNe, which could be too computationally expensive for numerical simulations to follow their entire pathways, the atmospheric elemental abundances in EMP stars have provided a unique observational probe to test theoretical predictions on the physical properties of the Pop III stars and their supernova explosions. Systematic searches with photometry and/or low-to-medium-resolution spectroscopy have identified a number of EMP star candidates (e.g., Beers & Christlieb 2005; Frebel & Norris 2015, and reference

therein). Follow-up high-resolution spectroscopy has determined detailed abundance patterns of the EMP stars, which allow us to study the typical properties of the first supernovae imprinted on their elemental abundances (Umeda & Nomoto 2003; Suda et al. 2008; Aoki et al. 2013; Cohen et al. 2013; Yong et al. 2013a; Roederer et al. 2014).

The following three results have been obtained so far. First of all, no metal-free stars have yet been found in the Milky Way, which suggests that the formation of lower-mass ($<0.8M_{\odot}$) Pop III stars that could survive until today was suppressed (Hartwig et al. 2015; Ishiyama et al. 2016; Magg et al. 2018). Second, no clear nucleosynthetic signatures of very massive stars $M \sim 140$–$300M_{\odot}$, such as a very high Si/O ratio resulting from a pair-instability supernova (Nomoto et al. 2013), have been found (see Aoki et al. 2014, for a candidate star). It should be noted, however, the current surveys may be biased against finding a star with nucleosynthetic signature of pair-instability Pop III supernovae because (i) a single pair-instability supernova would enrich all the gas within its reach to metallicities well above the EMP surveys, typically targeted at [Fe/H] < -3 (Karlsson et al. 2008), and (ii) pair-instability supernovae are so energetic (e.g., Heger & Woosley 2002; Umeda & Nomoto 2002) and occur in such low densities (e.g., Kitayama et al. 2004; Whalen et al. 2004) that their ejecta escape from the halo and would never been incorporated into the next generation of stars.

We also note that extremely massive stars ($300\,M_{\odot} < M < 10^5\,M_{\odot}$) enter the pair-instability region, but they continue to undergo gravitational collapse. Yields from jet-induced explosions of such stars were calculated by Ohkubo et al. (2006) and found to be consistent with the abundance patterns of intracluster medium—but not in good agreement with EMP stars (e.g., [O/Fe]).

Finally, the fraction of carbon-enhanced metal-poor (CEMP) stars increases with decreasing Fe abundance ([Fe/H]) (Yong et al. 2013b; Placco et al. 2014). The dominance of the CEMP stars among the lowest-[Fe/H] stars suggests that the characteristic abundance patterns observed in these stars reflect nucleosynthetic products of Pop III star's supernova explosions (Umeda & Nomoto 2002, 2003; Limongi et al. 2003; Meynet et al. 2006; Tominaga et al. 2007b; Heger & Woosley 2010; Ishigaki et al. 2014; Keller et al. 2014; Chen et al. 2017a) and their formation sites.

Interestingly, abundance patterns of EMP stars reported by previous observational studies (e.g., Cayrel et al. 2004; Lai et al. 2008) are well-explained by nucleosynthetic yields of individual or IMF-averaged core-collapse supernovae/hypernovae of Pop III stars in a range $\sim$10–100 $M_{\odot}$ with various explosion energies (Iwamoto et al. 2005; Tominaga et al. 2007b, 2014; Lai et al. 2008; Heger & Woosley 2010; Joggerst et al. 2010a; Placco et al. 2015). The 2D numerical simulations of Pop III supernovae with progenitor masses in a range 15–40 $M_{\odot}$ by Tominaga et al. (2007a), Tominaga (2009), and Joggerst et al. (2010a) also reproduce the observed elemental abundances reasonably well. Given the growing observational data for the EMP stars, the constraints on the Pop III star's masses should be statistically studied on the basis of on larger samples.

It is not straightforward, however, to accurately predict nucleosynthetic products finally ejected by the core-collapse supernovae of Pop III stars, i.e., supernova yields. The main reason for the uncertainty in the supernova yields is that the explosions could be highly non-spherical, as evidenced by both observations (e.g., Maeda et al. 2008) and theoretical calculations (e.g., Janka 2012; Kotake et al. 2012; Burrows 2013; Wongwathanarat et al. 2015). While the ejecta are determined by the progenitor star structure and the explosion energy, in the case of a spherical explosion, multi-dimensional calculations of mixing and fallback of the ejecta are needed to take the non-sphericity into account (Joggerst et al. 2009, 2010b).

In order to approximately account for the effects of the aspherical explosion in calculating supernova yields, the mixing-fallback model has been proposed by Umeda & Nomoto (2002). The mixing-fallback model mimics an aspherical explosion with three parameters, and is adopted on one-dimensional nucleosynthesis calculations of Pop III supernovae (see Appendix of Tominaga et al. 2007b). The resulting yields obtained from the model accurately reproduce the characteristic nucleosynthesis yields of aspherical explosions from two-dimensional simulations (e.g., Tominaga 2009; Joggerst et al. 2010a; Chen et al. 2017a) and successfully explain the key elemental abundances observed in EMP stars (Umeda & Nomoto 2002, 2003, 2005; Iwamoto et al. 2005; Tominaga et al. 2007b, 2014; Ishigaki et al. 2014; Kobayashi et al. 2014).

Given that the actual mechanisms of supernova explosions have not yet been established well (e.g., Janka 2012), the mixing-fallback model allows us to explore the parameter spaces that cover a wide range of mixing and fallback with much less computational cost than the multi-dimensional simulations. This enables us to obtain the typical properties of the Pop III stars by fitting the abundances of large statistical samples of EMP stars (see Section 2.2). The model also provides a framework to empirically constrain the degree of asymmetry, the ejected mass of radioactive ^{56}Ni (which powers the supernova lightcurve), and the mass of the compact remnant (either a neutron star or a black hole) left behind by the Pop III supernovae.

In this paper, we calculate a grid of the supernova yield sets of Pop III stars, using the mixing-fallback model, and we determine the best-fit model to reproduce each elemental abundance pattern in $\sim$200 EMP stars compiled from the recent literature. By applying the abundance fitting method to the large sample of EMP stars, we obtain the distributions of mass, the explosion energy, and the state of mixing and fallback of the Pop III supernova models. In the abundance fitting analysis, we take into account the theoretical uncertainties arising from stellar evolution and the supernova explosion mechanisms. We also examine the effects of observational uncertainties on the best-fit models, as well as on the inferred IMF of the Pop III stars. Based on the obtained best-fit models, we discuss the diagnostic elemental abundances that are sensitive to the Pop III masses, which will be useful in interpreting data from ongoing and future spectroscopic surveys of EMP stars.

This paper is organized as follows. In Section 2, we first describe our method to calculate the Pop III supernova yields. We describe the observational data of EMP stars from literature in Section 3. The results of the abundance fitting, the effects of observational uncertainties, and the comparison with literature are presented in Section 4; their implications are described in Section 5. Finally, we present a summary of the present analyses in Section 6.

Table 1
Properties of the Models

Model ID	M[a] ($M_\odot$)	E[b] (10^{51} erg)	$M_{\rm cut}$[c] ($M_\odot$)	$M_{\rm CO}$[d] ($M_\odot$)	Maximum $M_{\rm mix}$[e] ($M_\odot$)	Range of $M(^{56}{\rm Ni})$[f] ($M_\odot$)
13LE	13	0.5	1.47	2.39	3.30	1.55×10^{-8}–10^{-1}
13SN	13	1	1.47	2.39	3.30	1.67×10^{-8}–10^{-1}
15SN	15	1	1.41	3.02	4.64	1.32×10^{-8}–10^{-1}
25SN	25	1	1.69	6.29	10.90	2.61×10^{-8}–10^{-1}
25HN	25	10	1.69	6.29	10.90	6.72×10^{-8}–10^{-1}
40SN	40	1	2.42	13.89	25.36	5.18×10^{-8}–10^{-1}
40HN	40	30	2.42	13.89	25.36	1.96×10^{-7}–1
100SN	100	1	3.63	42.00	80.37	4.93×10^{-7}–1
100HN	100	60	3.63	42.00	80.37	8.13×10^{-7}–10

Notes.
[a] Progenitor mass.
[b] Explosion energy.
[c] Initial mass cut, which corresponds to the lower bound for the considered $M_{\rm mix}$ range.
[d] CO-core mass.
[e] Upper bound for the $M_{\rm mix}$ range.
[f] The range in ejected mass of ^{56}Ni for the parameter space considered in each model.

2. Abundance Fitting Method

2.1. Supernova Yields

We obtain nucleosynthesis yields of Pop III stars by making use of progenitor models and explosive nucleosynthesis previously calculated by Umeda et al. (2000), Iwamoto et al. (2005), Umeda & Nomoto (2005), and Tominaga et al. (2007b). The progenitor models were calculated through Fe core collapse for the initial masses of 13, 15, 25, 40, and 100 $M_\odot$. The Henyey-type stellar evolution code was used (Nomoto & Hashimoto 1988; Umeda et al. 2000, and references therein) with a nuclear reaction network as in Hix & Thielemann (1996). The abundance ratios of C, O, Ne, Mg, and Al in the core are largely influenced by the uncertain $^{12}{\rm C}(\alpha, \gamma)^{16}{\rm O}$ reaction rate (Fowler 1984; Chieffi & Limongi 2002), for which 1.4 times the value given in Caughlan & Fowler (1988) was adopted.

The explosive nucleosynthesis was calculated by injecting the thermal energy in the innermost region of the progenitor (Tominaga et al. 2007b). For the explosive burning, a reaction network that includes 280 species (up to ^{79}Br) is used, as in Umeda & Nomoto (2005).

We adopt nine pairs of progenitor initial masses (13, 15, 25, 40, and 100 $M_\odot$) and explosion energies (normal supernovae with $E_{51} = E/10^{51}\,{\rm erg} = 1$, low-energy supernovae with $E_{51} = 0.5$, and hypernovae with $E_{51} \geqslant 10$), as summarized in Table 1. In the following, we denote these models as 13LE for the low-energy supernova with the progenitor initial mass $M = 13\,M_\odot$, 13SN, 15SN, 25SN, 40SN, and 100SN for normal-energy supernovae with progenitor masses $M = 13$, 15, 25, 40, and 100 $M_\odot$, respectively, and 25HN, 40HN, and 100HN for hypernovae with progenitor masses $M = 25$, 40, and 100 $M_\odot$, respectively.

Among these massive stars, the 100 $M_\odot$ star undergoes pulsational pair-instability (PPI) and eventual Fe core collapse, which is common for 80–140 $M_\odot$ (e.g., Heger & Woosley 2002). One example of such an evolutionary track of the central density and temperature is seen in Figure 7 of Ohkubo et al. (2009) for the Pop III 135 $M_\odot$ star. Before PPI, the 135 $M_\odot$ star has much higher central entropy, compared to the 40 $M_\odot$ star at similar nuclear burning stages. PPI, however, delays the onset of Fe core collapse. As a result, the central entropy of the 135 $M_\odot$ star is decreased by neutrino emissions during PPI and becomes as low as that of the 40 $M_\odot$ star at the beginning of Fe core collapse (Figure 7 of Ohkubo et al. 2009). The hydrodynamical behavior of collapse of such a low-entropy Fe core after PPI has not been studied well. The supernova explosion and nucleosynthesis from such stars may not necessarily be only HN-like, but could also be normal-energy SN-like. Because there is no other empirical probe of the zero-metallicity supernova events, and recent cosmological simulations (e.g., Hirano et al. 2014) predict the formation of $\sim$100 $M_\odot$ Pop III stars, we include not only 100HN but also 100SN to investigate whether or not the signature of such a star is found in EMP stars. For each model, we apply the mixing-fallback model to calculate the supernova yields, as described in the next subsection.

2.2. The Mixing-fallback Model

In order to take into account the non-sphericity in supernova explosions, we apply the mixing-fallback model adopted in Umeda & Nomoto (2002, 2005) and Tominaga et al. (2007b). In this model, mixing of ejecta and the amount of fallback are described by the three parameters: the initial mass cut $M_{\rm cut}$, the outer boundary of mixing $M_{\rm mix}$, and the ejection fraction $f_{\rm ej}$. The $M_{\rm cut}$ represents the boundary, above which the nucleosynthesis products can potentially be ejected. The $M_{\rm mix}$ represents the outer boundary of the mixing zone, above which all materials are ejected. The fraction $f_{\rm ej}$ of the material contained in the mixing zone (i.e., the layers between $M_{\rm cut}$ and $M_{\rm mix}$) is finally ejected to the interstellar medium, while the remaining material falls back to the central compact remnant.

In our abundance fitting procedure, we fix $M_{\rm cut}$ at the surface of the Fe core, where the mass fraction of ^{56}Fe dominates over that of ^{28}Si in the pre-supernova progenitor, while $M_{\rm mix}$ and $f_{\rm ej}$ are free parameters. The adopted model properties are summarized in Table 1.

The outer boundary of mixing ($M_{\rm mix}$) is varied as a function of x, where $M_{\rm mix} = M_{\rm cut} + x(M_{\rm CO} - M_{\rm cut})$, in the range of $x = 0.0$–2.0 with a stop of 0.1. The range of $M_{\rm mix}$ is thus from $M_{\rm cut}$ up to $M_{\rm cut}$+2.0($M_{\rm CO} - M_{\rm cut}$). The ejection fraction $f_{\rm ej}$ is logarithmically varied from $\log f_{\rm ej} = -7$ to 0, with a step of 0.1 dex. Based on the best-fit parameters, we also calculate the

mass of the compact remnant left behind following the fallback, based on the following relation from (Tominaga et al. 2007b):

$$M_{\rm rem} = M_{\rm cut} + (1 - f_{\rm ej})(M_{\rm mix} - M_{\rm cut}) \quad (1)$$

2.3. Abundance Fitting Procedure

From the grid of SN yields for the nine models with varying parameters in Table 1, the best-fit models are searched by minimizing $\chi^2_\nu = \chi^2/\nu$. Here, the degree of freedom, ν, refers to the value $\nu = N - M$, where N and M are the number of abundance data points and the number of parameters (mass, energy, $M_{\rm mix}$, $f_{\rm ej}$ and the hydrogen mass), respectively. The χ^2 is defined below, similarly to that employed in Heger & Woosley (2010),

$$\chi^2 = \sum_{i=1}^{N} \frac{(D_i - M_i)^2}{\sigma_{o,i}^2 + \sigma_{t,i}^2} + \sum_{i=N+1}^{N+U} \frac{(D_i - M_i)^2}{(\sigma_{o,i}^2 + \sigma_{t,i}^2)} \Theta(M_i - D_i) + \sum_{i=N+U+L}^{N+U+L} \frac{(D_i - M_i)^2}{(\sigma_{o,i}^2 + \sigma_{t,i}^2)} \Theta(D_i - M_i), \quad (2)$$

where D_i and M_i are observed and model values of [X/H], respectively, and for an element i, $\sigma_{o,i}$ and $\sigma_{t,i}$ are corresponding to observational and theoretical uncertainties, respectively. The Heaviside function $\Theta(x)$ is defined to be $\Theta(x) = 1$ for $x > 0$, and 0 otherwise. The observational upper (lower) limits are only taken into account if these limits are below (above) the model values via the second (third) term in the above expression. The theoretical lower limit, described in 2.4, is implemented in the second term with the same expression as the observational upper limit. In this analysis, the hydrogen mass to calculate [X/H] abundance in the model is also varied as a free parameter, to take into account a wide range of [Fe/H] for the second-generation stars predicted by hydrodynamical simulations (e.g., Ritter et al. 2012).

For C and N abundances, we fit the combined value [(C+N)/H], rather than treating [C/H] and [N/H] separately, for two reasons. First, atmospheric abundances of evolved EMP stars might have been affected by internal mixing, through which material from the H-burning shell is dredged up. Because C is processed into N in the H-burning shell via CNO cycle, the surface abundances with the internal mixing would have been enhanced in N, at the expense of C. Second, the above process could have also occurred within the progenitor Pop III star before its supernova explosion. Therefore, the combined C+N abundance is not significantly affected, although the individual C and N abundances may have changed from the original value.

2.4. Theoretical Uncertainties

The theoretical uncertainties stem from physical mechanisms that are treated approximately (overshooting, etc.) or are not taken into account (stellar rotation and/or ν-process, etc.) in the employed model. We discuss these limitation in more detail in Section 5.5.

Among the elements mainly produced during the stellar evolution, Na and Al are known to be subject to several uncertainties. Because these elements are synthesized in the C-shell burning via the reaction ^{12}C(^{12}C, p)^{23}Na(α, γ)^{27}Al, the Na and Al abundances are sensitive to the ^{12}C abundance after core He burning and the temperature of the C-shell burning. They depend on the ^{12}C(α, γ)^{16}O reaction rate (Chieffi & Limongi 2002) and the overshooting (Iwamoto et al. 2005). For these reasons, we assume a larger theoretical uncertainty ($\sigma_{t,i}$) of 0.5 dex for Na and Al.

Titanium and scandium are known to be underproduced in one-dimensional calculations of supernova nucleosynthesis, compared to those observed in EMP stars (e.g., Tominaga et al. 2007b; Sneden et al. 2016). Several possible sites have been proposed for their synthesis, such as the neutrino process (Kobayashi et al. 2011a) and/or the jet-induced explosions (Tominaga 2009, and references therein). Because the main production sites have not been clearly identified due to the uncertainties in the physical mechanisms of supernovae, we treat the model abundances of Ti and Sc as lower limits. For the other elements, the theoretical uncertainties are assumed to be zero.

3. Abundance Data from Literature

We employ the elemental abundance data available from recent studies for large samples of EMP stars (Cohen et al. 2013; Yong et al. 2013a; Roederer et al. 2014; Jacobson et al. 2015) and newly identified UMP stars (Hansen et al. 2014; Frebel et al. 2015; Placco et al. 2015, 2016; Meléndez et al. 2016). These studies are selected so that the abundance measurements of C, N, O, Na, Mg, Al, Si, Ca, Sc, Ti, Cr, Mn, Fe, Co, Ni, and Zn have been performed based on high-resolution spectra with a spectral resolution greater than $R \sim 28{,}000$. Some EMP stars are analyzed in more than one reference, for which we take the data from the study with the largest number of measured elemental abundances.

In the following analysis, we restrict our sample to EMP ([Fe/H] < -3) stars, which were presumably formed out of gas predominantly enriched by a single supernova. With the [Fe/H] criterion, the number of unique stars is 219. To examine whether a star is likely polluted by an evolved AGB binary companion, we check their Sr and Ba abundances. Three stars in the sample have [Sr/Fe] > 1, but none of them show [Ba/Fe] > 1. Therefore, we keep these stars in our sample.

In the abundance fitting analysis, we consider abundances relative to the solar abundance of Asplund et al. (2009) ([X/H]) of C+N, O, Na, Mg, Al, Si, Ca, Sc, Ti, Cr, Mn, Fe, Co, Ni, and Zn. Among these elemental abundances, [Fe/H] abundances are measured from the largest number of absorption lines, and thus we assume the smallest error of 0.1 dex in the abundance fitting analysis. In most of the literature data, C and N abundances have been measured from spectral fitting of CH and CN molecular features and are known to be sensitive to the 3D effects in the stellar atmosphere (e.g., Gallagher et al. 2016). In this paper, we adopt 0.2 and 0.3 dex for the uncertainties of [C/H] and [N/H], respectively. Significant non-LTE effects are expected for O abundances measured from IR OI triplet lines at 777 nm, Na abundances from Na I D doublet and Al abundances from Al I 3961 Å line (Baumueller & Gehren 1997; Fabbian et al. 2009; Lind et al. 2011), which are adopted in most of these studies. In particular, the non-LTE (NLTE) correction to the Al abundances ranges from ~0.2 dex up to ~0.6 dex for EMP stars, depending on stellar atmospheric parameters. In the following analysis, except for the three stars with [Fe/H] < -5 in Section 4.6, we use uncorrected values for the O, N, and Al abundances, but

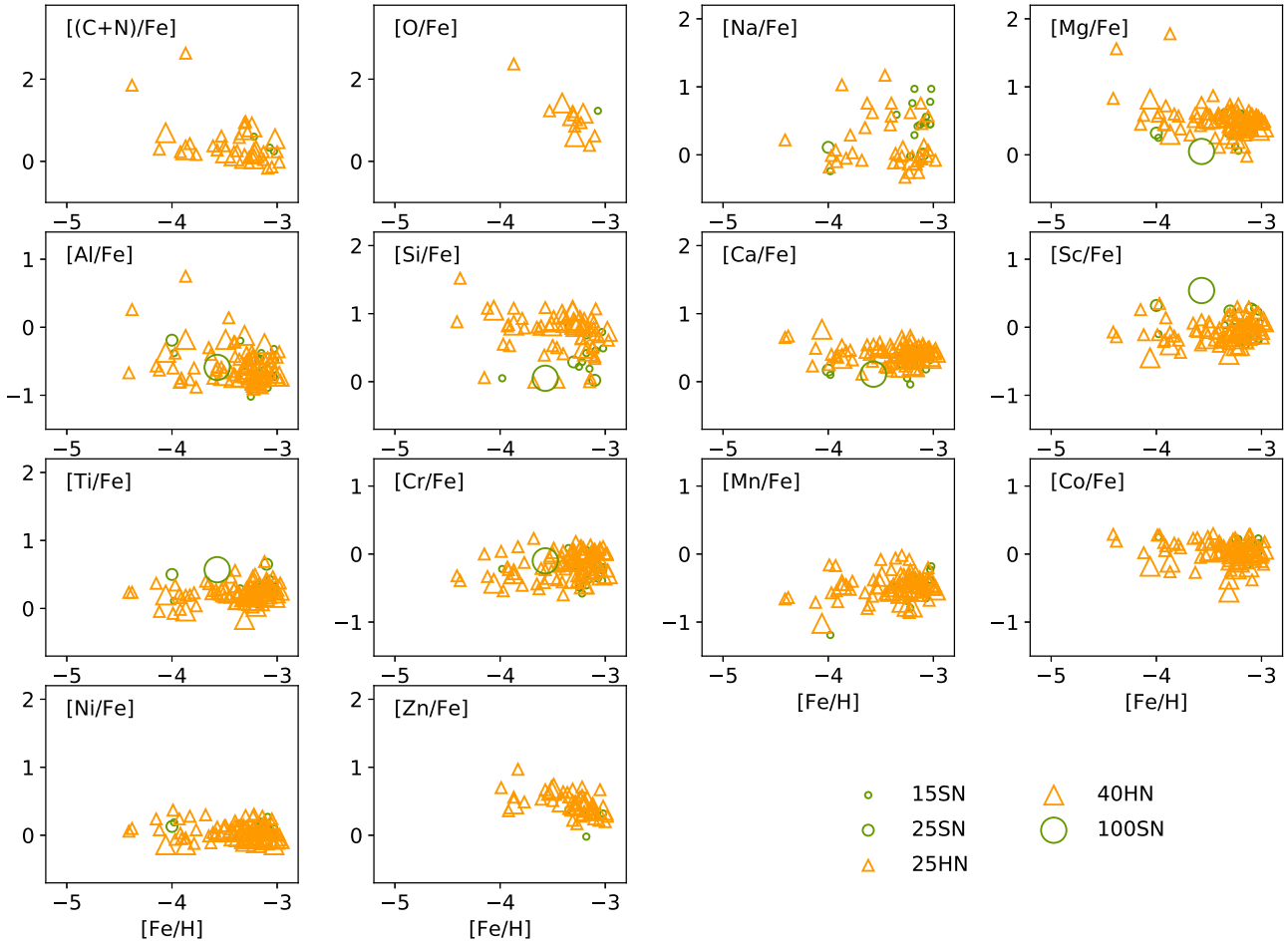

Figure 1. Observed abundance ratios ([X/Fe]) of the present sample of EMP stars that are fitted by the models with $\chi^2_\nu < 3$, plotted against [Fe/H]. Symbols indicate the best-fit models (either 15SN, 25SN, 25HN, 40HN, or 100SN models) for individual stars. The symbols' meanings are shown in the lower-right corner.

assign a relatively large error of 0.3 dex for these elements. In most of the studies, Si abundances are determined from only one or a few lines, and we adopt a larger error of 0.2 dex. The large errors of 0.2 dex are also assigned to the Ti and Cr abundances because their abundances from neutral and ionized species generally disagree by 0.1–0.5 dex in 1D-LTE analyses (Kobayashi et al. 2006; Roederer et al. 2014). A relatively large error of 0.2 dex is also assigned to Mn abundances because they are most frequently measured from the resonance lines at ∼4030 Å and the derived Mn abundances have been reported to disagree with the values from non-resonance lines by ∼0.3 dex (e.g., Cohen et al. 2013). For the other elements, an observational uncertainty of 0.15 dex is assumed. In the following analysis, we restrict our sample to those having observed [X/H] constraints (excluding upper limits) greater than seven, to make sure that the five model parameters (mass, energy, $M_{\rm mix}$, $f_{\rm ej}$, and hydrogen mass) are well-constrained. We differ our discussion on the three most Fe-poor stars, HE 0107-5240 (Christlieb et al. 2002), HE1327-2326 (Frebel et al. 2005; Aoki et al. 2006), and SMSS 0313-6708 (Keller et al. 2014), based on the most recent abundance measurements for these stars in Section 4.6.

4. Results

As a result of the abundance fitting described in the previous sections, the $M = 15\,M_\odot$/supernova (15SN), $25\,M_\odot$/supernova (25SN), $25\,M_\odot$/hypernova (25HN), $40\,M_\odot$/hypernova (40HN), or $100\,M_\odot$/supernova (100SN) models best-fit with $\chi^2_\nu < 3$ the abundance patterns of at least one EMP star. The best-fit $13\,M_\odot$/low-energy (13LE) or $100\,M_\odot$/hypernova (100HN) models are also found, but they result in larger χ^2_ν values. The best fits were not found for the 13SN or 40SN models. The observed abundances ([Fe/H] and [X/Fe]) and their best-fit models (one of the 15SN, 25SN, 25HN, 40HN, or 100SN models) are summarized in Figure 1 and Table 3 in the Appendix (published entirely in an electronic form).

In our analysis, we have checked whether there is only one best-fit peak or more than one local χ^2 minimum in the parameter space. Figures 2 and 3 show the example plots, where we plot the behavior of a p-value, which is calculated as an integral of a χ^2 probability distribution of a given degree of freedom above the observed χ^2 value, in the planes of the model parameters. The nine different panels correspond to the nine models (Table 1) considered in this work. Each panel plots the p-values by colors in the $\log f_{\rm ej} - x$ space, where x is the scale factor for $M_{\rm mix}$ (see Section 2.2 definition).

We confirm that the region with the largest p-values is found only around the best-fit parameter (shown by a cross) and no secondary minima are found for the $\log f_{\rm ej} - x$ parameter space of a given model. The distinctions between the different models are, however, not always clear. For example, for the case of CS 22941-017 (Figure 2), the region with larger p-values is located at $\log f_{\rm ej} > -2$ and $x < 0.5$, not only in the best-fit model (25HN), but also in other models, such as the 40HN model. To take into

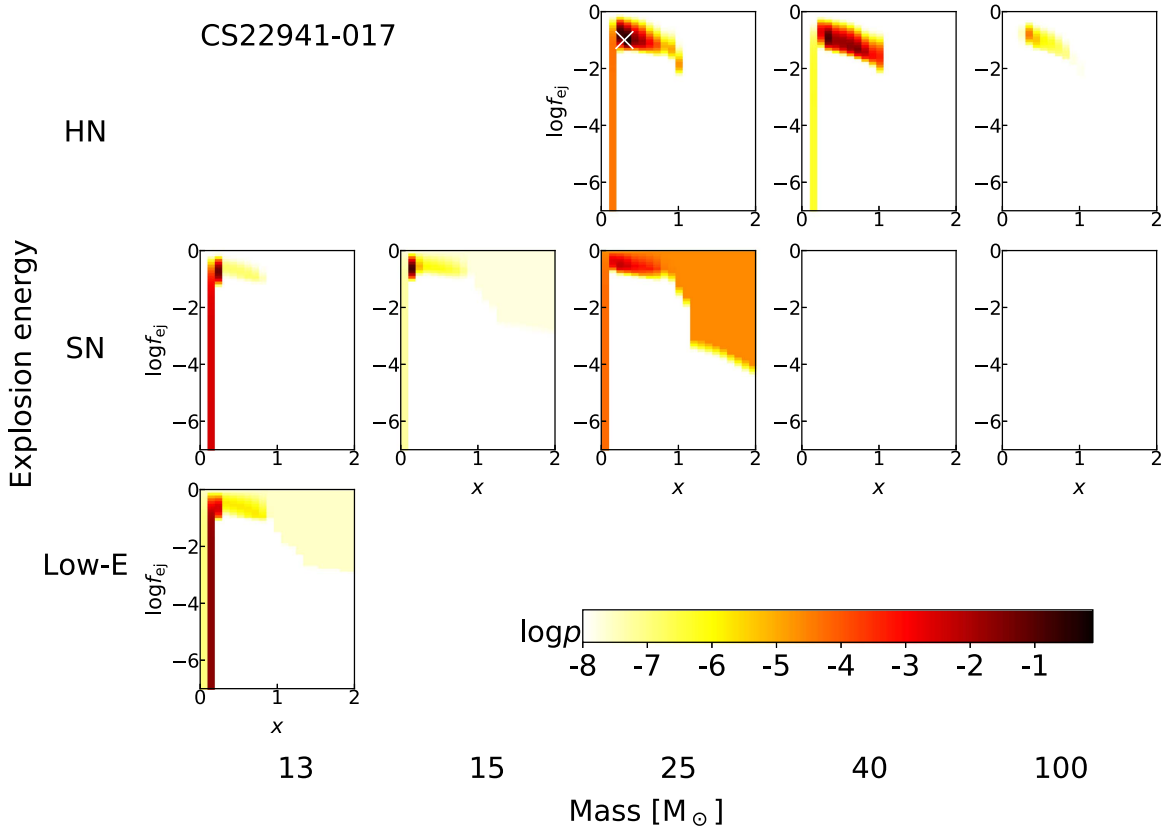

Figure 2. Distribution of the p-values calculated as an integral of χ^2 probability distribution for a given degree of freedom in the parameter spaces for one of the EMP stars, CS22941-017. Different panels correspond to the models with various progenitor masses (increasing along the horizontal axis) and explosion energies (increasing along the vertical axis; from bottom to top, low-energy or "LE," normal-energy or "SN," and high-energy or "HN" explosions). Each panel shows the p-values in a $\log f_{\rm ej} - x$ plane, where x is the scale factor of $M_{\rm mix}$ (see Section 2.2). The location marked by a white x indicates the best-fit parameters.

account such cases where multiple models have similar p-values for a given star, we show our results with and without the p-value weighting in Section 4.2. In addition, we investigate the effects of observational and theoretical uncertainties on the resulting inference on the masses of the models in Section 4.3. For the case of CS 29498-043 (Figure 3), for which all of the abundance measurements considered in the present analysis are available, higher p-values are only seen around the best-fit parameters in the 25HN model.

To illustrate the characteristic abundance patterns of the models of the different masses and the explosion energies, Figure 4 shows the best-fit models (15SN, 25SN, 25HN, 40HN, and 100SN from top to bottom) and the observed abundances for the stars fitted with relatively small χ^2_ν. It can be seen that the odd–even effect among Na, Mg, Al, and Si abundances is stronger in the $M = 25\,M_\odot$/supernova model than in the $M = 15\,M_\odot$/supernova model.

In the following subsections, we describe the [X/Fe] ratios of the best-fit models for each of the 15SN, 25SN, 25HN, 40HN, and 100SN models.

4.1. Characteristic Abundance Ratios

The left panels of Figures 5 and 6 show observed abundances of stars (circles) and the best-fit models (solid and dotted lines) for the cases of $\chi^2_\nu < 5$. From top to bottom in the two figures, the stars that are best-fitted by the 15SN, 25SN, 25HN, 40HN, and 100SN models are shown. The right panels show histograms for the best-fit $M_{\rm mix}$ and $f_{\rm ej}$ values and the resultant remnant masses ($M_{\rm rem}$) and ejected ^{56}Ni masses for each model.

4.1.1. Stars Fitted with the 15SN Model

Figure 5(a) shows the observed abundances and the best-fit $M = 15\,M_\odot$/supernova (15SN) models. As mentioned before, the best-fit 15SN models are characterized by relatively small differences in abundance ratios between neighboring odd and even atomic-number elements among Na to Si, compared to the other mass/energy models. In particular, the difference between [Na/Fe] and [Mg/Fe] ratios is small, compared to the other models.

As illustrated in Figure 5(b), the $M_{\rm mix}$ parameter is peaked at $\sim$1.6 $M_\odot$, which approximately corresponds to the outer boundary of the Si layer in the post-supernova structure. The $f_{\rm ej}$ parameter is peaked at $\log f_{\rm ej} \sim -0.5$, which indicates that $\sim$30% of the mass contained in the mixing zone ($M_{\rm cut} - M_{\rm mix}$) is finally ejected and left as the mass fallback to the compact remnant. As a result, as shown in the bottom two panels of Figure 5(b), the mass of the compact remnant is predominantly $\sim$1.5 $M_\odot$, which corresponds to a neutron star, and the ejected mass of ^{56}Ni is in the range of 0.01–0.1 $M_\odot$.

4.1.2. Stars Fitted with the 25SN Model

Figure 5(c) shows the observed abundances and the best-fit $M = 25\,M_\odot$/supernova models (25SN). Compared to the 15SN model, the [Na/Fe] ratios are lower and predominantly subsolar. Also, on average, the [Ni/Fe] ratios are higher for the stars fitted with the 25SN model than for those fitted with the 15SN model.

Figure 5(d) demonstrates that the large fraction of these stars are fitted with $M_{\rm mix} \sim$ 2–4 $M_\odot$, which corresponds to the inner

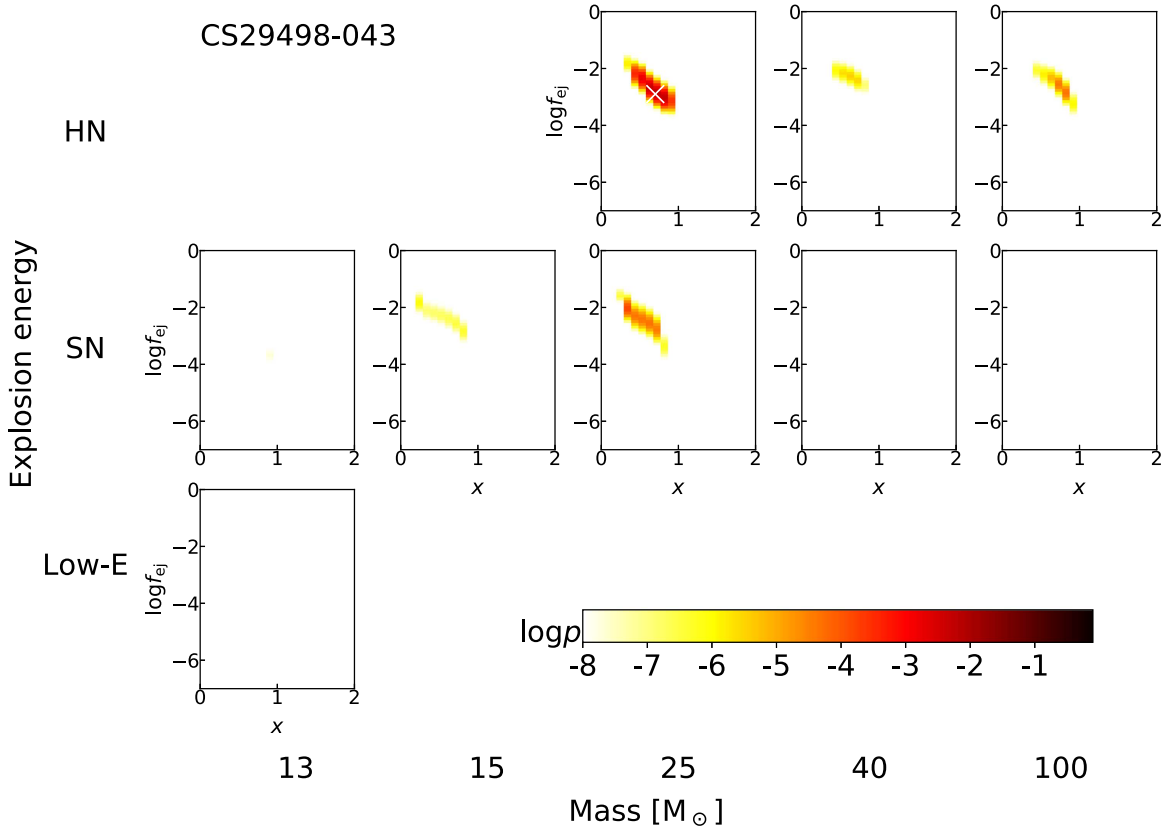

Figure 3. Same as Figure 2, but for a CEMP star, CS 29498-043.

boundary of Si layer up to the inner part of the CO core in the post-supernova structure. The ejected fraction is 0.01–0.5, which results in compact remnants of 2–4 $M_\odot$, which generally corresponds to a black hole. The ejected ^{56}Ni mass is 0.01–0.1 $M_\odot$, similar to those seen in the 15SN model.

4.1.3. Stars Fitted with the 25HN Model

About half of the sample stars are best-fitted with the $M = 25\,M_\odot$/hypernova models (25HN), which are shown in Figure 5(e). On average, the [Si/Fe], [Co/Fe], and [Zn/Fe] ratios are larger for the best-fit 25HN models than for the best-fit 25SN models.

Figure 5(f) shows that a large fraction of stars are fitted with $M_{\rm mix} \sim 3\,M_\odot$, which approximately corresponds to the outer boundary of the Si-burning layers in the post-supernova structure. The ejected fraction is 0.01–0.5, which results in remnant masses of 2–4 $M_\odot$ and an ejected Ni mass of 0.01–0.1 $M_\odot$.

Compared to the 25SN models, the 25HN models have more extended regions for the explosive burning and thus result in larger productions of Si. Consequently, with the similar remnant masses, the ejected Si abundances are larger for the 25HN model. Also, the explosive Si burning produces larger amounts of Co and Zn in the more energetic explosions, which better fit the observed high [Co/Fe] and/or [Zn/Fe] ratios.

4.1.4. Stars Fitted with the 40HN Model

Figure 6(a) shows the observed abundances and the best-fit $M_\odot = 40\,M_\odot$/hypernova models (40HN). In contrast to the stars best-fitted with the 25HN model, most of the stars do not have Na measurements, which allows the best-fit models to have a very low (<-0.5) [Na/Fe] ratio.

Figure 6(b) shows that, in most cases, the $M_{\rm mix}$ parameters are below $\sim 6\,M_\odot$, which corresponds to the outer boundary of the Si layer. The ejection fractions are peaked at $\log f_{\rm ej} = 0.1$, resulting in the remnant mass of $\sim 6\,M_\odot$, which indicates the formation of a black hole after the hypernova. The ejected ^{56}Ni mass is $\sim 0.1\,M_\odot$, which is broadly in agreement with those estimated for nearby hypernovae of stars with a main-sequence mass $\sim 40\,M_\odot$ (Nomoto et al. 2006).

4.1.5. Stars Fitted with the 100SN Model

Only two stars in our sample (HE 0130-2320 and HE 0218-2738) are best-fitted with the 100SN models, one of which has $\chi^2_\nu < 3.0$. The observed abundances and the best-fit models are shown in Figure 6(c). The abundances of these stars are characterized by [Mg/Fe] and [Si/Fe] ratios of $\sim 0.0 \pm 0.1$, which are lower than typical metal-poor stars. We should note that the Ni and Zn abundance measurements are not available for these stars, which results in best-fit models with very low [Ni/Fe] and [Zn/Fe] ratios (~ -0.5 dex). Thus, in order to confirm the characteristic abundance patterns expected from the 100SN model, additional abundance measurements for Ni and Zn are crucial. In fact, if the 100SN model is dropped from the grid of yields, as this model is not theoretically motivated (see Section 2.1), the two stars are alternatively best-fitted with the 25HN models, which predict [Zn/Fe] $\sim$ 0.3 dex.

As shown in Figure 6(d), the best-fit parameters for the two stars are $M_{\rm mix} = 46$ and $34\,M_\odot$ and $f_{\rm ej} = 10^{-6}$ and 0.16, respectively. The corresponding remnant masses are 46 and $29\,M_\odot$, respectively, which suggests the formation of a black hole with these masses.

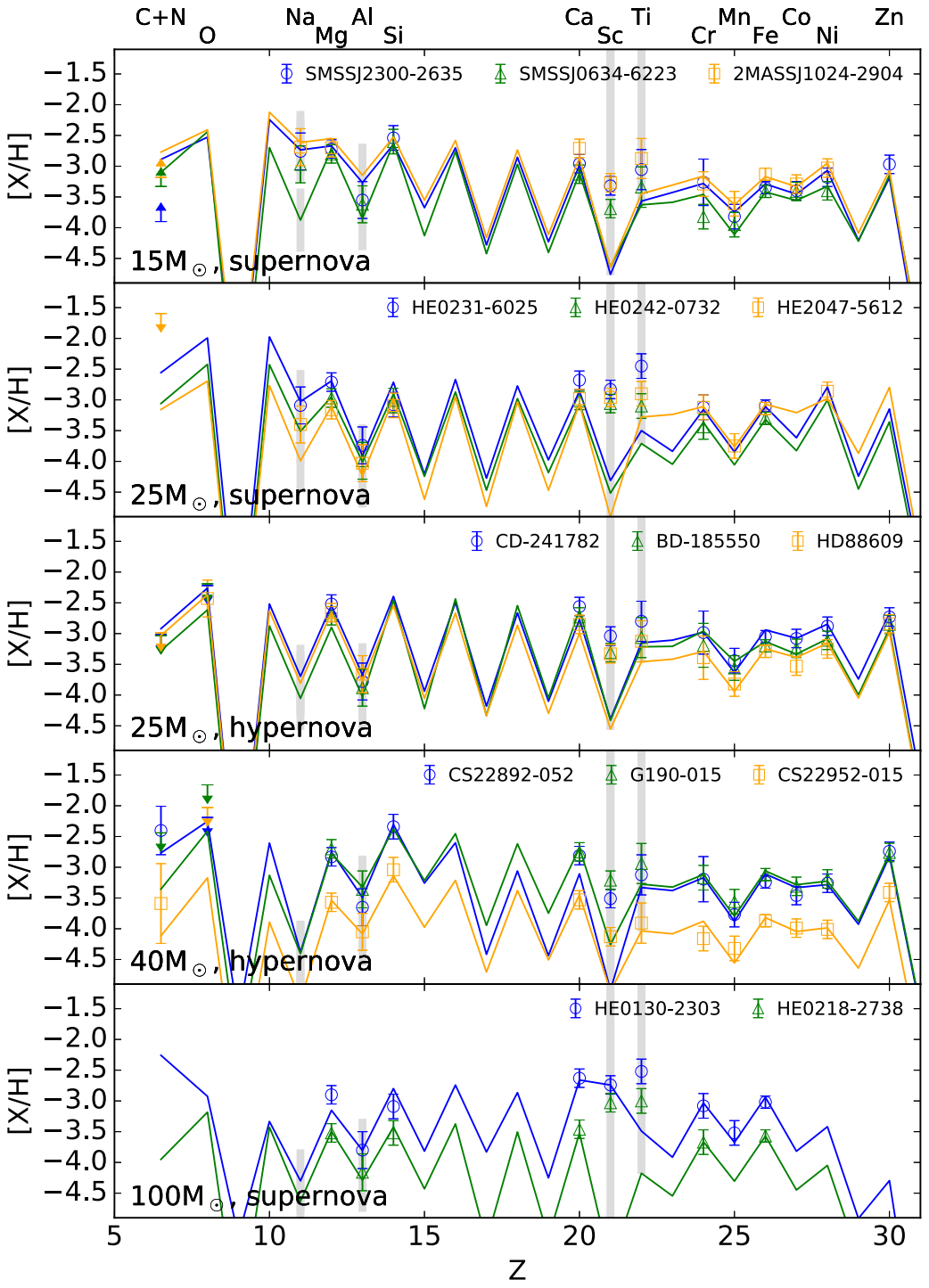

Figure 4. Observed abundances (circle, triangle, and square with error bars, arrows for upper limits) and the best-fit models (solid lines with color corresponding to each star) for stars with relatively small χ^2_ν among those fitted with each of the five models. From top to bottom, the stars best-fitted with the 15SN, 25SN, 25HN, 40HN, and 100SN models, respectively, are shown. The model abundances of elements marked by gray bars are either assigned a large theoretical uncertainty (Na and Al) or treated as a lower limit (Sc and Ti).

4.1.6. Other Models

In our sample, stars that are best-fitted with the 13SN or 40SN models are not found, and two objects are best-fitted with the 13LE or 100HN models but with $\chi^2_\nu > 3$. Figure 7 shows example for the fitting of these models. It can be seen that the 13SN model (top panel) under-produces the [Na/Fe] ratios while they overproduce [Al/Fe]. The 40SN models also predict higher [Al/Fe] than the observed values.

4.1.7. CEMP

In our sample, 18 stars are CEMP stars with [(C+N)/Fe] $>$ 1.0. Similarly to the other stars, the CEMP stars are

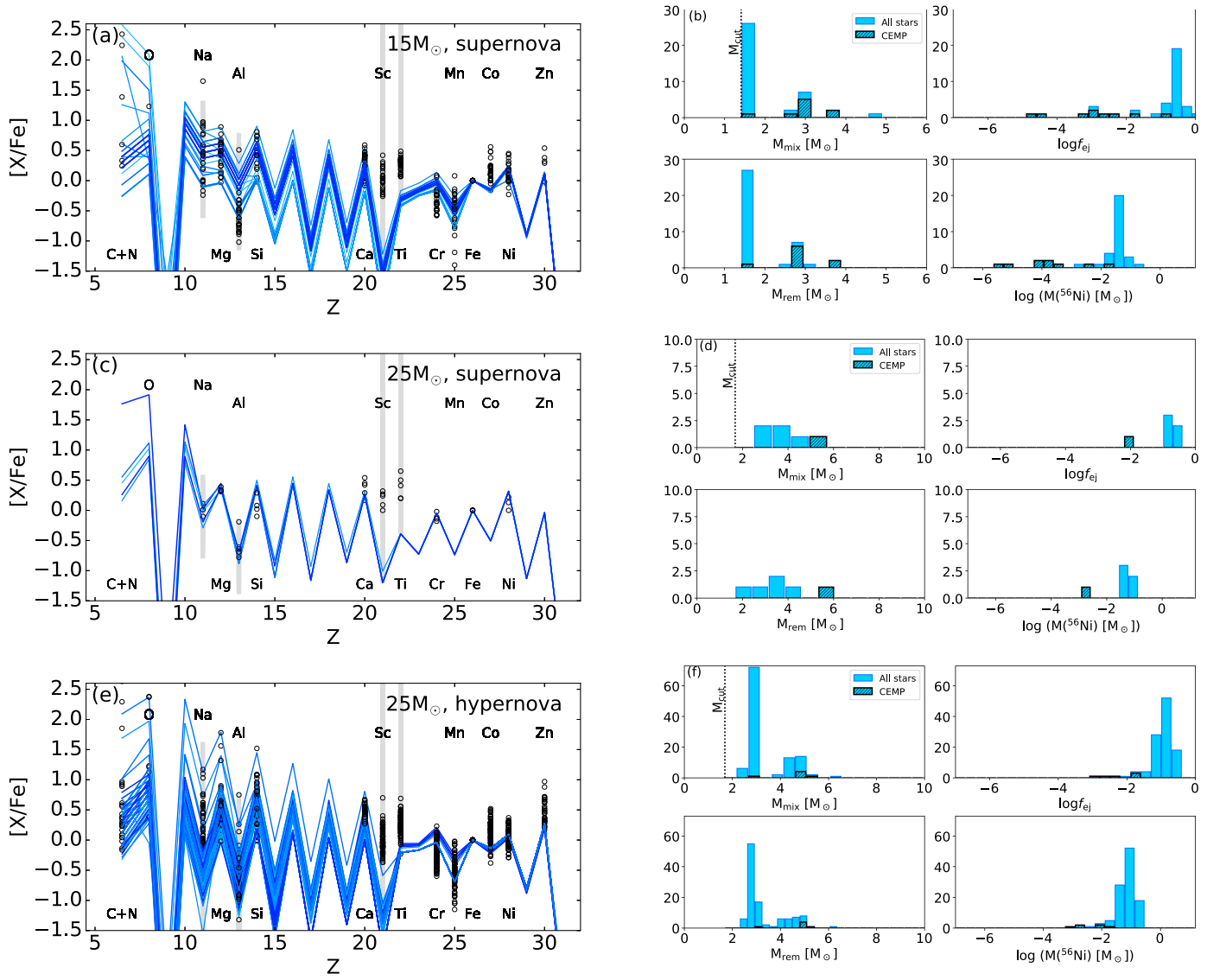

Figure 5. Left column: abundance patterns of the stars best-fitted with (from top to bottom) the 15SN, 25SN, and 25HN models. The black circles indicate the observational data. The solid lines show the best-fit models where darker colors represents smaller χ^2_ν. Right column: the top two panels show distributions of the best-fit $M_{\rm mix}$ and $\log f_{\rm ej}$ parameters of the models shown in the left column. For the $M_{\rm mix}$ parameter, the vertical lines indicate the value of $M_{\rm cut}$. The bottom two panels show distributions of the resulting mass of the compact remnant ($M_{\rm rem}$; Equation (1)) and the ejected ^{56}Ni mass. The hatched histogram is for the CEMP stars.

predominantly best-fitted with either the 15SN, 25SN, or 25HN models. Figure 8 shows the best-fit models for the 12 CEMP stars with $\chi^2_\nu < 5$. Their abundances require models with a larger-scale mixing and fallback than those required for the other EMP stars; the $M_{\rm mix}$ is much larger than the outer boundary of the Si layers and the $f_{\rm ej} < 0.1$. Consequently, the compact remnants of the CEMP progenitors span the highest mass range in the remnant mass distribution, as can be seen in Figure 5(b), (d), and (f).

The C+N enhancements in the CEMP stars are sometimes associated with enhancements of Na, Mg, or Al abundances. In our analysis, stars with [Mg/Fe] > 1 (CS 22949-037, CS 29498-043, and HE 1012-1540) are best-fitted by the 25HN models while those with lower [Mg/Fe] ratios are fitted with either the 13LE, 15SN, or 25SN models. The requirement for high explosion energy stems from the fact that Mg is explosively synthesized at the bottom of the He layer ($M_r \sim 5.5\,M_\odot$). Consequently, in order to reproduce the high [(C+N)/Fe] ratios, the layer containing these explosively synthesized Mg should be ejected in the model, which explains both the high [(C+N)/Fe] and [Mg/Fe] ratios.

4.2. Pop III Masses and Explosion Energy

As mentioned earlier, the observed abundances of the EMP sample stars are explained best by the models for Pop III stars with masses $M = 15$, 25, 40 or $100\,M_\odot$ that explode with normal ($E_{51} = 1$) or higher explosion energies ($E_{51} > 1$). In this section, we examine the typical masses of the first stars whose nucleosynthetic products are incorporated into the EMP stars.

The left panel of Figure 9 shows the histogram of the Pop III masses of the best-fit models. Blue, green, and orange bars correspond to the low-energy, normal-energy, and hypernovae explosion models, respectively. In order to include the contributions from models other than the best-fit ones, the right panel of Figure 9 shows the histogram we obtained by counting contributions from all nine models weighted by the

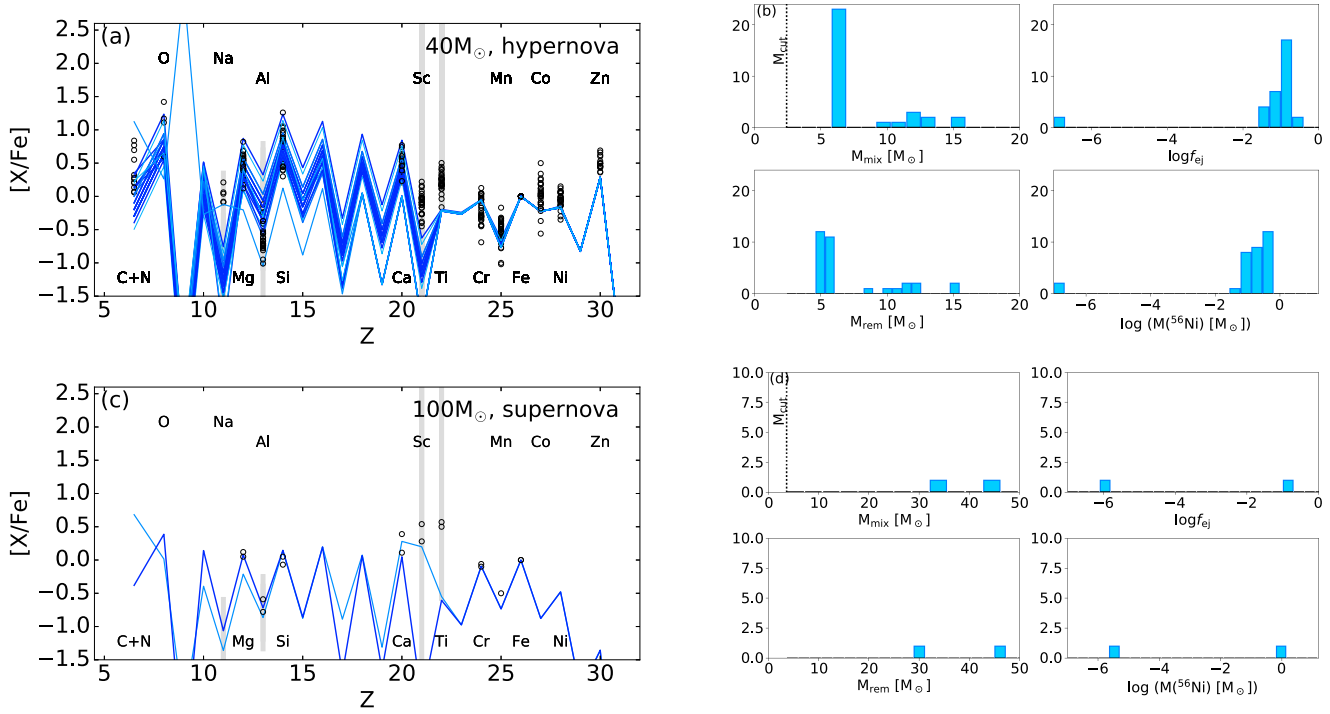

Figure 6. Same as Figure 5, but for the 40HN and 100SN models.

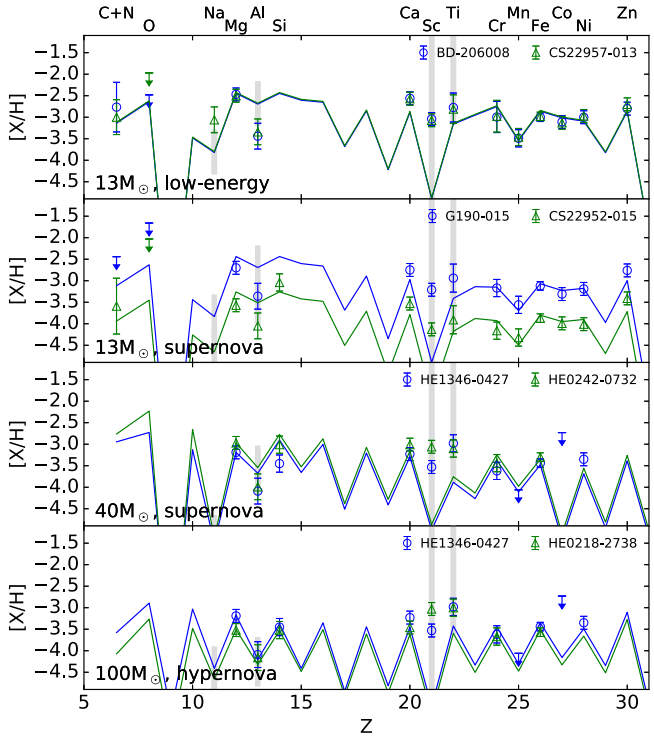

Figure 7. Abundance patterns of the 13LE, 13SN, 40SN, or 100HN models, which do not best-fit the data for any of the present sample stars. The data are shown by symbols with error bars, and the models with relatively small χ^2_ν are shown by solid lines with colors corresponding to the data.

p-values as Cp, where the constant C is set so that these weights sum to unity for each star.

It can be seen from both histograms that the highest contribution comes from the $M = 25\,M_\odot$ models, and more than half of the whole stars are best explained by the $M = 25\,M_\odot$/hypernova model. The Pop III masses for the progenitors of the CEMP stars, shown by the hatched histograms, also dominate at $M \leqslant 25\,M_\odot$, while relative contribution from $M = 15\,M_\odot$ Pop III models are larger than the $M = 25\,M_\odot$ models. Given the theoretical and observational uncertainties, we found it difficult to clearly distinguish the $M = 15$ and $25\,M_\odot$ models. Therefore, the Pop III progenitors of the CEMP are not clearly distinct, in terms of masses, from those of the majority of the EMP stars. This result implies that the physical mechanism of the formation of CEMP stars is rather related to the state of the mixing and fallback (e.g., Figure 5), which presumably occur in aspherical supernova/hypernova explosions.

4.3. Robustness of the Best-fit Progenitor Masses

4.3.1. Effects of Observational Uncertainties

We examine the robustness of the fitting results against the fiducial observational errors assigned to the data (0.1–0.3 dex; see Section 3). For this test, we select objects with $\chi^2_\nu < 1$ among those best-fitted with each of the 15SN, 25SN, 25HN, 40HN, 100SN, and 100HN models. For each of the selected objects, the same abundance fitting procedure is performed 100 times by adding noises taken from a Gaussian distribution with a sigma (standard deviation) equal to the adopted observational errors.

The blue histogram in each panel of Figure 10 shows the distribution of the best-fit progenitor mass/energy models obtained from the 100 abundance-fitting runs. From top to bottom, the panels show results for the objects originally best-fitted with the 15SN, 25SN, 25HN, 40HN, 100SN, and 100HN models.

For some of the adopted observational errors, a different progenitor mass/energy model is chosen as the best-fit. For the case of SMSS J065014.40-614328.0, which was originally best-fitted with the 15SN model, a different model, either

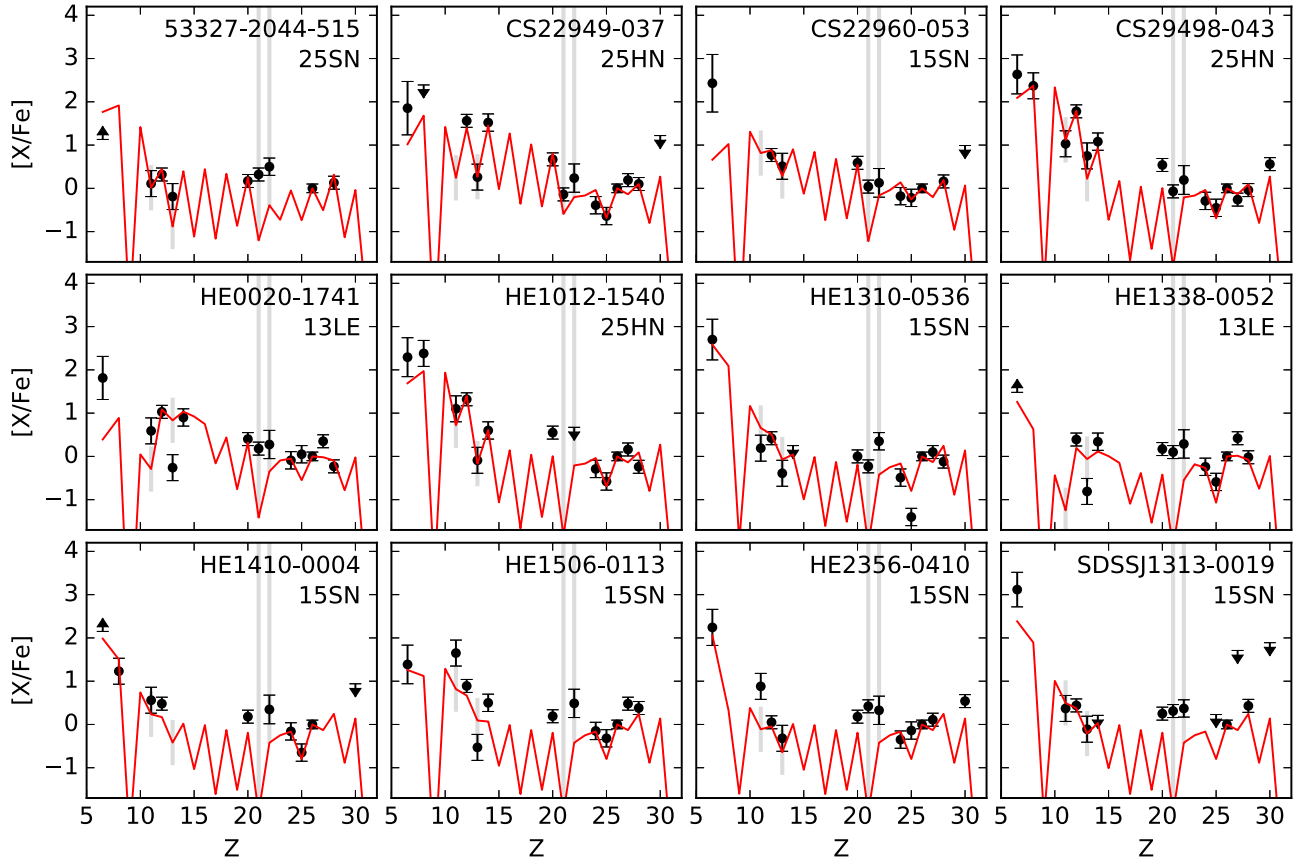

Figure 8. Best-fit models for the CEMP stars with $\chi^2_\nu < 5$.

13LE, 13SN, 25SN or 25HN, best-fits the data more than 50 times. The probability of getting other models as the best-fit is also high for an object fitted with the 25SN model (HE 0242-0732), for which there is a ∼40% probability of obtaining the 100SN model as the best fit. On the other hand, for objects best-fitted with the 25HN, 40HN, or 100SN models, the original best-fit models are chosen with $\gtrsim$50% probability.

These results suggest that, for the fiducial observational errors adopted as in Section 3, the best-fit models are not always robustly determined, especially for objects best-fitted with the 25SN model. On the other hand, the objects best-fitted with the 25HN, 40HN, or 100SN models tend to have distinct abundance patterns, so that they are more robustly distinguished.

The recovery of the original fit is improved when the adopted observational errors are half the fiducial value (0.05–0.15 dex), as shown by the red histograms in Figure 10. All but one of the objects are fitted by the original best-fit models for more than 50% of the runs. Therefore, reducing the observational errors is crucial to obtain tighter constraints on the progenitor-mass distributions of Pop III stars in our analysis.

4.3.2. Effects of Systematic Uncertainties

One of the major systematic uncertainties in measured abundances comes from the NLTE effect on Al abundances, for which suggested NLTE correction is up to ∼+0.6 dex. The effect of change in measured Al abundances is tested by repeating the same abundance-fitting procedures, but adding 0.6 dex to the Al abundances measured under the assumption of LTE as a NLTE correction. The resultant progenitor-mass histogram and the histogram obtained by weighting with the p-value are shown in the top two panels in Figure 11. As can be seen from the top-left panel, some fraction of stars that have originally been fitted with the 25HN model are now better fitted with either the 13SN or 15SN models. This can be understood because the elevated Al abundance via the NLTE correction gives a smaller odd–even effect, and thus is better fitted with a lower progenitor mass model, as mentioned in Section 4.1.1. Therefore, the weighted histogram in the top-right panel shows that the contribution from $M \leqslant 15\,M_\odot$ is larger than that of $M = 25\,M_\odot$, in contrast to the original histogram. This results highlight the importance of obtaining the NLTE abundances for Al in order to discriminate the progenitor Pop III masses between $M \leqslant 15$ and $25\,M_\odot$ in observations.

Another possible source of systematic uncertainties is missing observational data for certain elements on the Pop III masses. For example, as can be seen from the bottom panel of Figure 4, the objects fitted with the 100SN model tend to have a smaller number of elements measured in observations than the stars fitted with the other models. This might imply that the finding of the best fit with the 100SN models could stem from the non-measurements of particular elements. In order to test the robustness of the Pop III mass histogram against the number of constraints, the bottom two panels in Figure 11 plot the same histogram as in Figure 9, but only for stars where the abundance constraints (either measurements or upper limits) are available for all the elements we chose (C, N, O, Na, Mg, Al, Si, Ca, Sc, Ti, Cr, Mn, Fe, Co, Ni, and Zn). This reduces the sample stars to only 15. The resulting histogram for the best-fit model is shown in the bottom-left panel, and the corresponding

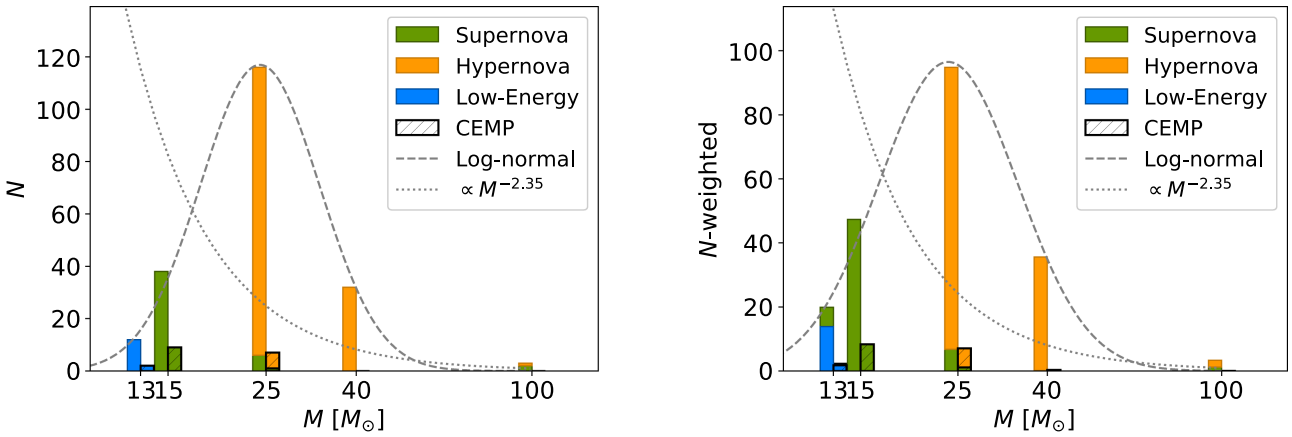

Figure 9. Left: the histogram of the Pop III progenitor masses of the best-fit models. Green, orange, and blue bars correspond to supernova, hypernova, and low-energy explosion models, respectively. The results for the CEMP star are shown by hatched bars. The gray dashed line shows the best-fit log-normal function to the histogram. For a reference, the Salpeter IMF ($\propto M^{-3.5}$), arbitrarily normalized for better visibility, is shown by a dotted line. Right: the histogram obtained by counting contributions from all nine mass-energy models weighted by the p-value (see the text for the definition).

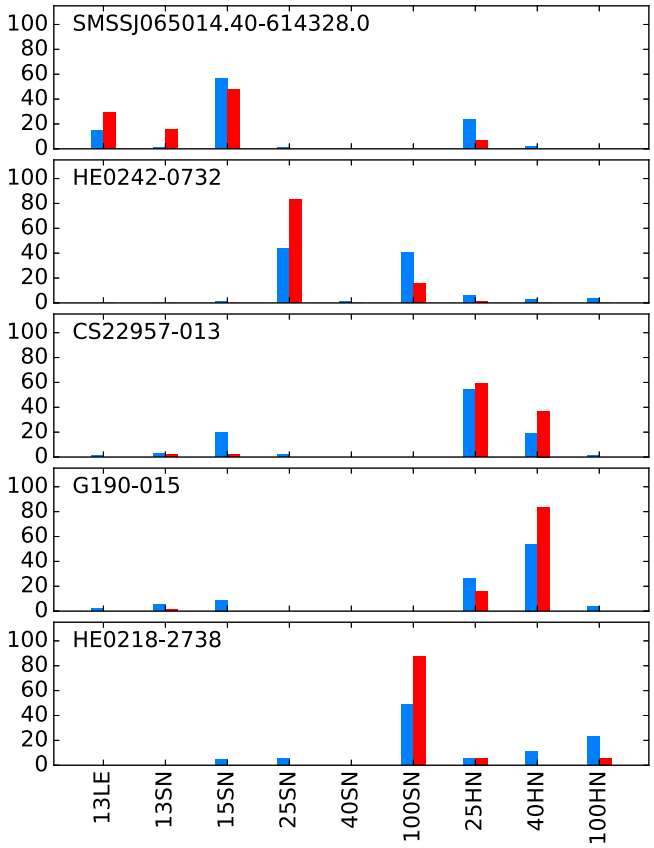

Figure 10. Distributions of the best-fit models obtained from the 100 abundance-fitting runs by adding noises from the observational errors. From top to bottom, the panels show results for objects originally best-fitted with the 15SN, 25SN, 25HN, 40HN, and 100SN models (SMSS J065014.40-614328.0, HE 0242-0732, CS 22957-013, G 190-15, and HE 0218-2738). The blue histograms show the results for the fiducial observational errors (0.1–0.3 dex), assigned as described in Section 3. The red histograms show the results when half of the fiducial errors are assigned.

p-value-weighted histogram is shown in the bottom-right panel. Both histograms show that the Pop III masses are peaked at $25\,M_\odot$ and that the contribution from the 15SN models is suppressed, compared to the histogram for the whole sample (Figure 9). It can be seen, however, that the main results on the Pop III masses, namely, the mass distribution being dominated by $M < 40\,M_\odot$ and peaking at $M = 25\,M_\odot$, are robust against the number of abundance constraints in our analysis.

To further test the non-measurement of a specific element in our abundance fitting, we select stars that have the measurements of all 16 elements we chose. In our sample, only one star, CS29498-043, has a complete abundance measurement. We perform the abundance fitting by excluding elements one-by-one, then comparing the results to the original best-fit model ($M = 25\,M_\odot$ and $E_{51} = 10$). With this experiment, except for the cases omitting Si or Zn, the original best-fit model is reproduced—but with slightly different mixing-fallback parameters. The lack of Si measurement leads to a best-fit model with a higher progenitor mass ($M = 40\,M_\odot$) and a higher explosion energy ($E_{51} = 30$). On the other hand, the lack of Zn measurement leads to a best-fit model with the same progenitor mass and a lower explosion energy ($E_{51} = 1$), as expected. This experiment demonstrates that the best-fit model does not change even if we omit one of the abundance measurements, except for Si or Zn. Therefore, in our analysis, abundance measurements of Si and Zn are particularly important in constraining the Pop III models.

4.4. Comparisons with Previous Studies

Placco et al. (2015) fit supernova yields of Pop III stars to a sample of 20 ultra-metal-poor stars using the publicly available code, *STARFIT*, which is based on the grids of yields calculated by Heger & Woosley (2010). Although *STARFIT* also takes into account the mixing-fallback process, an assumption in the code is different from ours. In *STARFIT*, the supernova explosions are treated as if they are close to being rather spherically symmetric, and the Rayleigh–Taylor instability and spherical fallback are assumed to be the main mixing-fallback mechanisms. On the other hand, we consider various degrees of asymmetry in the explosions, including those associated with a jet and fallback along the equatorial plane.

The comparison for 10 stars analyzed in common is summarized in Table 2. Placco et al. (2015) obtained best-fit Pop III models ranging from $M = 10.9$ to $28\,M_\odot$ with explosion energies $E_{51} = 0.3$–10.0. The range of progenitor masses is broadly consistent with the results obtained with our analysis (15 or $25\,M_\odot$).

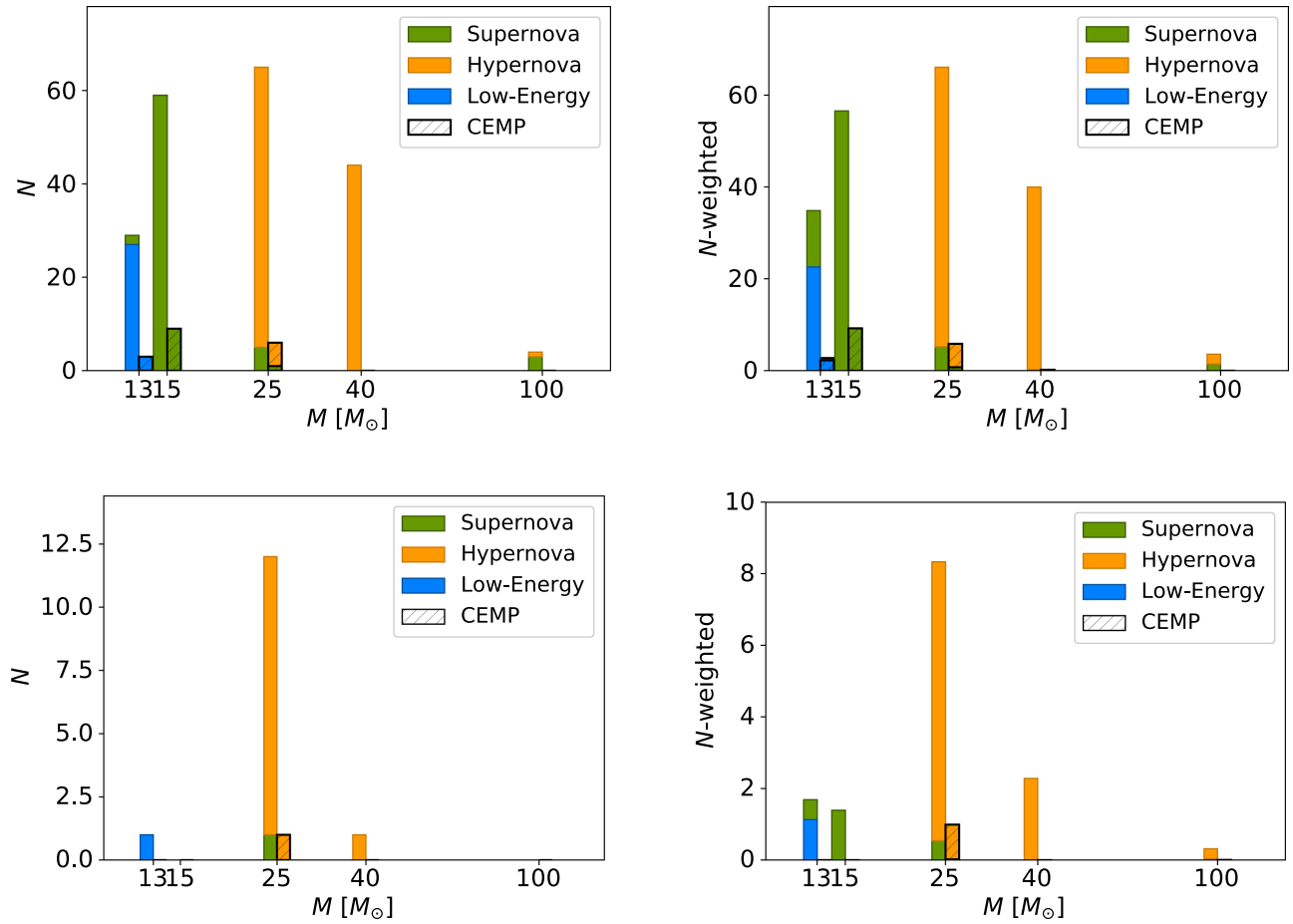

Figure 11. Top: same as Figure 9, but for the result of the abundance fitting after the uniform NLTE correction to the observed Al abundance is applied. Bottom: same as Figure 9, but only for objects whose abundance measurements or upper limits of all the elements we chose are available.

Table 2
Comparison with Placco et al. (2015)

Star name	[Fe/H]	[C/Fe]	Placco+15				This work			
			M ($M_\odot$)	E (10^{51} erg)	$M_{\rm rem}$[a] ($M_\odot$)	$M(^{56}{\rm Ni})$[b] ($M_\odot$)	M ($M_\odot$)	E (10^{51} erg)	$M_{\rm rem}$ ($M_\odot$)	$M(^{56}{\rm Ni})$ ($M_\odot$)
					[C/Fe] < 1					
CS 30336-049	−4.03	+0.09	21.5	0.3	7.88	7.66×10^{-5}	15	1	1.49	6.9×10^{-2}
HE 1424-0241	−4.05	+0.63	21.5	0.3	7.88	7.66×10^{-5}	15	1	2.01	3.4×10^{-2}
CD-38 245	−4.15	−0.09	21.5	0.3	7.88	7.66×10^{-5}	25	10	2.96	5.4×10^{-2}
SDSS J1204+1201	−4.34	<+1.45	10.6	0.9	1.41	NA	25	1	2.38	6.8×10^{-2}
					[C/Fe] > 1					
HE 2139-5432	−4.02	+2.60	28.0	0.6	9.51	3.36×10^{-4}	25	10	4.91	8.6×10^{-4}
HE 2239-5019	−4.15	+1.80	15.0	10.0	1.43	1.06×10^{-1}	25	1	2.72	6.8×10^{-2}
HE 1310-0536	−4.15	+2.53	10.9	0.3	1.59	9.49×10^{-3}	15	1	2.86	1.7×10^{-4}
CS 22949-037	−4.38	+1.73	27.0	0.3	12.03	2.01×10^{-5}	25	10	3.05	8.6×10^{-2}
HE 0557-4840	−4.75	+1.66	10.9	0.6	1.41	1.28×10^{-2}	40	30	9.94	1.2×10^{-1}
SDSS J1313-0019	−5.00	+2.96	27.0	0.3	12.03	2.01×10^{-5}	25	1	5.36	8.5×10^{-4}

Notes.
[a] Remnant mass for given progenitor mass and explosion energy taken from Zhang et al. (2008).
[b] Ejected mass of ^{56}Ni for given progenitor mass and explosion energy of the mixed model from Heger & Woosley (2010).

Differences in explosion energies can be seen in some of these stars. For example, explosion energies are lower in Placco et al. (2015) than in our study for many of the stars listed in Table 2. In the *STARFIT* code applied in Placco et al. (2015), the amount of fallback is coupled to the explosion energy based on 1D hydrodynamical simulations by Zhang et al. (2008), and thus the low explosion energy is required for the larger fallback (Heger & Woosley 2010). For example, Pop III SNe with $E_{51} \leqslant 0.6$ result in larger fallback, leaving behind compact remnants with larger masses. The mixing is assumed to result from Rayleigh–Taylor mixing and is parameterized by a fraction of the He core mass, $f_{\rm mix}$ corresponding to a width of a

box-car smoothing kernel for the abundance structure. The difference is also partly due to the limited progenitor mass and energy coverage necessary to allow a wider range of the mixing and fallback parameters in the present study.

Table 2 also lists the inferred mass of the compact remnant and the ejected mass of ^{56}Ni from Zhang et al. (2008) and Heger & Woosley (2010). The remnant masses are systematically higher in Placco et al. (2015), ranging from $\sim$1.5 $M_\odot$ for M = 10–15 $M_\odot$ progenitor models and $\sim$7.9–12.0 $M_\odot$ for $M > 20\,M_\odot$ progenitor models. On the other hand, the remnant masses in our study range from $M = 1.5$ to 5.0 $M_\odot$. The ejected ^{56}Ni masses are smaller, with $M(^{56}\mathrm{Ni}) < 10^{-3}\,M_\odot$, in Placco et al. (2015), while they are typically $M(^{56}\mathrm{Ni}) = 10^{-4}$–$10^{-1}\,M_\odot$ in the present analysis.

4.5. Stars with Large χ^2_ν Values

In the present sample, the abundance fitting for the eight objects results in $\chi^2_\nu > 8.5$. The observed abundance ratios ([X/Fe]) and their best-fit models are shown in Figure 12. These stars can be broadly classified into two categories, based on their characteristic abundance ratios, as detailed below.

4.5.1. Stars with a Very Low [Si/Fe] Ratio

The top two panels in Figure 12 show the observed abundances and the best-fit models for HE 1424-0241 and HE 0251-3216, both of which have extremely low [Si/Fe] ratios (-1.0 and -0.7, respectively). Both objects show [Mg/Fe] ratios similar to other EMP stars, and thus very low [Si/Mg] ratios. Despite the similarity in [Si/Mg] between the two stars, their [(C+N)/Fe] and [Ca/Fe] ratios are largely different: HE 1424-0241 shows a very low [Ca/Fe] ($\leqslant -0.5$) ratio, and there is no sign of carbon enhancement (Cohen et al. 2007, 2013). Tominaga (2009) suggests that the abundance ratios of this star are well-reproduced by angle-delimited yields calculated for a jet-induced supernova of a population III 40 $M_\odot$ star. On the other hand, HD 0251-3216 is a C-enhanced star with [C/Fe] ratio $\sim$2.5 and shows a normal [Ca/Fe] ratio (Cohen et al. 2013). Although there are no Sr measurements, both the [Y/Fe] and [Ba/Fe] ratios are relatively high (>1 dex), and thus contribution from AGB nucleosynthesis cannot be ruled out. For both stars, however, the low [Si/Fe] ratios remain challenging for the theoretical calculations to reproduce.

4.5.2. Stars with Very High [Co/Fe]

Remaining six stars (CS 29527-015, HE 0017-4346, HE 2215-2548, HE 1402-0523, HE 2135-1924, and SMSSJ005953.98-594329.9) all show a much higher [Co/Fe] ratio (>0.5) than that typically observed in other EMP stars. The high [Co/Fe] ratio is not attributed to the NLTE effects in the abundance analysis because the correction is positive, and thus it would increase the discrepancy further from the theoretical yields (Bergemann et al. 2010). These stars show a variety of abundances for the other elements. As an example, HE 0017-4346 is a CEMP star with [(C+N)/Fe] > 1 and an enhancement of both [Na/Fe] and [Mg/Fe] ratios. The abundance pattern of this star is marginally fitted with the 15SN model, with a small ejected mass of ^{56}Ni. HE 2215-2548 shows enhancements of both [Co/Fe] and [Zn/Fe] ratios (>0.5 dex). As discussed in Tominaga (2009), the high-entropy environment realized in a simulation of jet-induced supernova

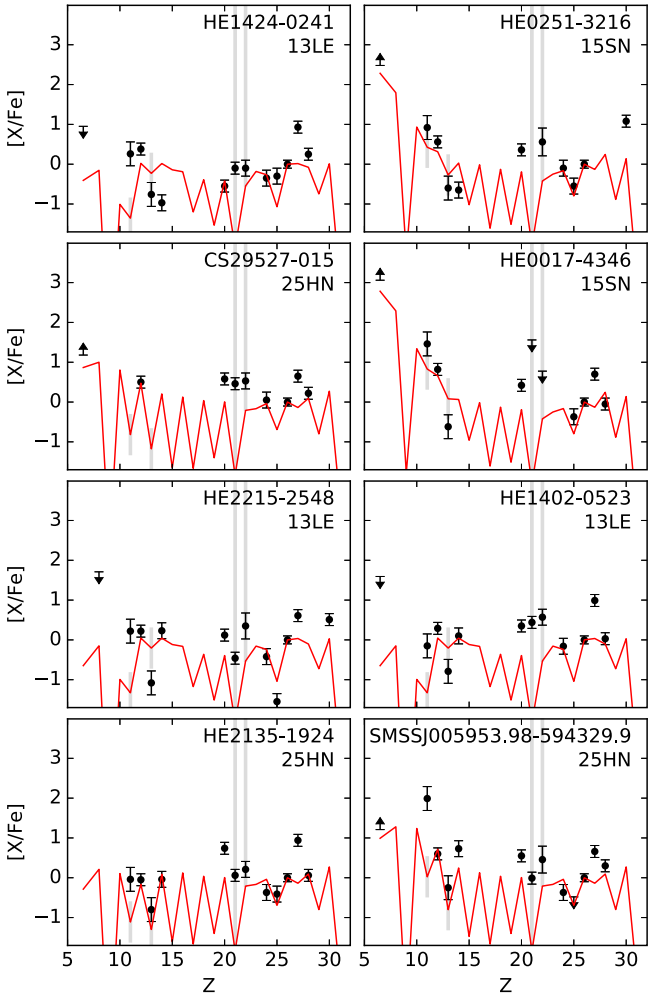

Figure 12. Model and observed abundance patterns for stars whose best-fit models have $\chi^2_\nu > 8.5$.

enhances Co and Zn, but still underestimate the observed abundances.

4.6. Hyper Metal-poor Stars with [Fe/H] < −5

The three most Fe-poor ([Fe/H] < −5) stars, HE 0107-4240 (Christlieb et al. 2002; Collet et al. 2006), HE 1327-2326 (Frebel et al. 2005; Aoki et al. 2006; Frebel et al. 2008), and SMSS 0313-6708 (Keller et al. 2014; Bessell et al. 2015; Nordlander et al. 2017) are not included in the main sample because the numbers of reported elemental abundances are small in the references used for the other sample stars (see Section 3). For these three stars, we use chemical abundances derived from 3D and/or NLTE analyses when available, mainly from Collet et al. (2006), Frebel et al. (2008), and Nordlander et al. (2017). For these three stars, the abundance fitting method is applied by separately treating C and N abundances with theoretical uncertainties of 0.5 dex. Because [Fe/H] has not been obtained for SMSS 0313-6708, the hydrogen mass is varied to reproduce the observed [Ca/H] abundances rather than [Fe/H].

The resulting best-fit models for HE 0107-5240 and HE 1327-2326 are shown in the top and the middle panels of Figure 13. The abundances of both stars are best-fitted with the model for a Pop III star with $M = 15\,M_\odot$ which explodes with a normal explosion energy ($E_{51} = 1$). The best-fit mixing-fallback model

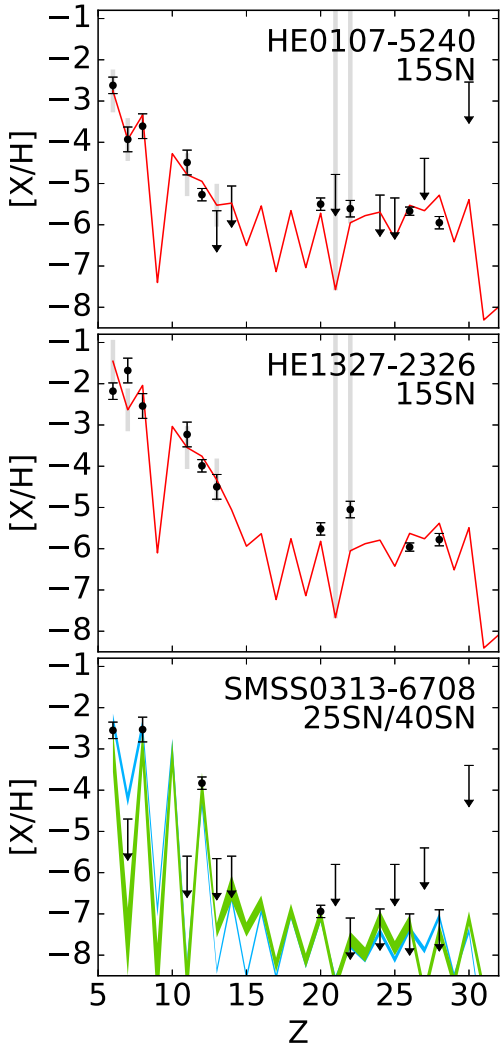

Figure 13. Best-fit models and observed abundances for the stars with [Fe/H] < -5. The top two panels show the best-fit 15SN models and the observed abundances for HE 0107-5240 and HE 1327-2326. The bottom panel shows observed abundances and upper limits for SMSS 0313-6708 and the ranges spanned by the models that fit the data with $\chi^2 < 10$, which are either the 25SN (blue band) or 40SN (green band) models.

parameters for these two stars suggest that they leave behind a compact remnant with $M = 2.9\,M_\odot$ and eject a very small amount of ^{56}Ni ($<10^{-4}\,M_\odot$).

For SMSS 0313-6708, abundance measurements for only C, O, Mg, and Ca are available, while upper limits for other elements have been obtained either from 1D/3D LTE or 3D/NLTE analyses (Bessell et al. 2015; Nordlander et al. 2017). The ranges spanned by the models with χ^2 smaller than 10 are shown in the bottom panel of Figure 13. As a result of the abundance fitting, only the 25SN ($M = 25\,M_\odot$ and $E_{51} = 1$; blue band) or 40SN ($M = 40\,M_\odot$ and $E_{51} = 1$; green band) models fit the data with $\chi^2 < 10$. Among them, the low upper limit for the [N/H] abundance is consistent with the 40SN model. The progenitor mass of $40\,M_\odot$ is similar to that suggested by Bessell et al. (2015), based on the *STARFIT* code (Heger & Woosley 2010); the model for a $40\,M_\odot$ Pop III star that explodes with $E_{51} = 1.8$ and modest mixing explains the observed abundance pattern. The origin of Ca in the models of Bessell et al. (2015) and this work, however, is different; namely, Ca in the model of Bessell et al. (2015) is produced in the outer layer by the hot-CNO cycle during the pre-supernova evolution, while it is produced by static/explosive O and Si burning in the model presented in this work (Ishigaki et al. 2014). While the new abundance constraints from 3D-NLTE abundance analysis by Nordlander et al. (2017) are consistent with the latter scenario, as shown in the bottom panel of Figure 13, additional abundance measurements, especially for Fe-peak elements, are necessary to distinguish between the two Ca production scenarios. Because the hot-CNO cycle can occur only in a zero-metallicity star, the origin of Ca in SMSS 0324-6708 could be an important diagnostic to examine whether or not the progenitor of this star has to be a Pop III star.

5. Discussion

5.1. Implications on the Initial Mass Function of the Pop III Stars

One of the major goals of this study is to derive the IMF of the first stars from the observed elemental abundances of EMP stars. We note, however, that the mass function we obtain in this abundance fitting analysis is the IMF of the first metal-enriching stars, which are not necessarily the same as the IMF of the first stars. In Section 4.2, we show that, among the adopted Pop III supernova models (low-energy explosion for $13\,M_\odot$; SNe for 13, 15, 25, 40, and $100\,M_\odot$; and HNe for 25, 40, and $100\,M_\odot$ Pop III stars), the majority of the EMP stars with available abundance measurements are best explained by the models of Pop III stars with masses 15 and $25\,M_\odot$ (Figure 9). The mass function of the first metal-enriching stars is well represented by a log-normal function,

$$\propto \exp(-(\ln x - \mu)^2 / 2\sigma^2) \quad (3)$$

with $(\mu, \sigma) = (3.28 \pm 0.02,\ 0.31 \pm 0.01)$ for the non-weighted histogram and $(3.30 \pm 0.03,\ 0.36 \pm 0.02)$ for the weighted histogram.

More specifically, at $M = 13$ or $15\,M_\odot$, the Pop III models fitting observed abundances are ~50% less frequent than at $M = 25\,M_\odot$. This is different from the Salpeter IMF, which has a power-low form of $M^{-2.35}$, as shown in the dotted lines in Figure 9. The NLTE correction to the Al abundances increases the contribution from the $M = 13$ and $15\,M_\odot$ models, but the $M = 25\,M_\odot$ model remains dominant in the histogram, as shown in Figure 11.

Similarly, at $M \geqslant 40\,M_\odot$, the best-fit Pop III models are about one-third of those of the $M = 25\,M_\odot$. The smaller contribution from the larger Pop III mass ($M \geqslant 40\,M_\odot$) implies that either (1) the formation mechanism of the first stars inhibit the formation of $\gtrsim 40\,M_\odot$ stars, (2) the first stars with $\gtrsim 40\,M_\odot$ directly collapse into a black hole remnant without ejecting any nucleosynthetic products, or (3) the supernova explosions of higher-mass first stars inhibit the formation of the next-generation stars (e.g., Cooke & Madau 2014).

Stacy & Bromm (2013) took into account the formation of multiple stellar systems in their cosmological simulation and found that the maximum Pop III mass is limited to $M \sim 40\,M_\odot$. This mass range is consistent with scenario (1), where the formation of $M \geqslant 40\,M_\odot$ Pop III stars is inhibited. On the other hand, Hirano et al. (2014) predict abundant formation of more massive stars ranges, from $M = 10\,M_\odot$ up to a few thousands of $M_\odot$, by taking into account statistical variation of the properties of primordial star-forming clouds in a cosmological

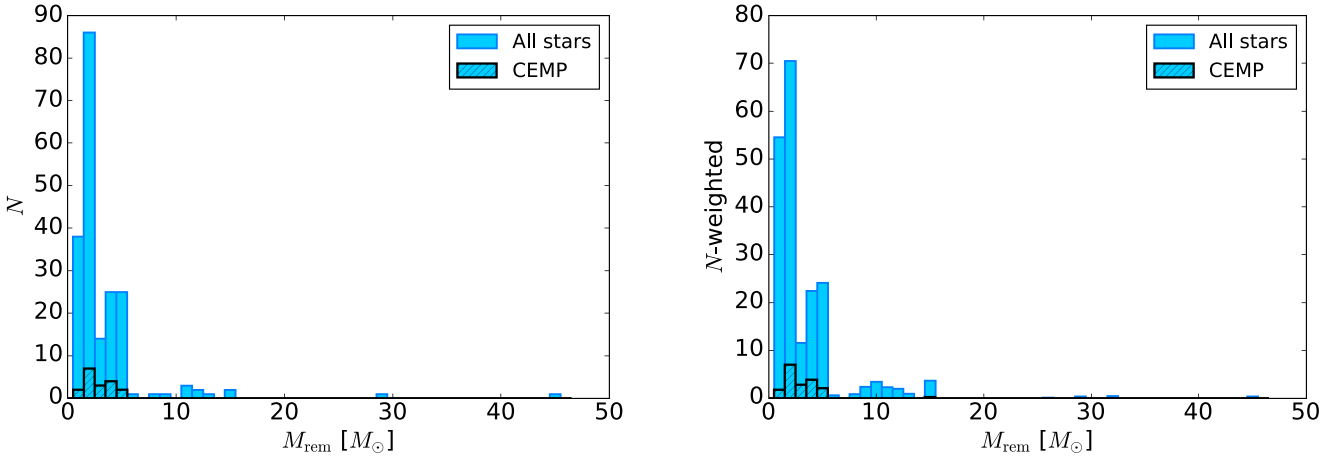

Figure 14. Left: a histogram of the remnant mass $M_{\rm rem}$ obtained by Equation (1) from the best-fit parameters for each star. Right: the corresponding histogram obtained by counting contributions from all the mass-energy models weighted by the p-values. The hatched histograms correspond to the histograms for the CEMP stars.

context (see also Hirano & Bromm 2017). Using three-dimensional radiation hydrodynamics simulations, Susa et al. (2014) also predicts a similar but slightly lower mass range for the Pop III stars ($1 \lesssim M \lesssim 300\,M_\odot$). These two results are more in line with scenario (2), where the Pop III stars with $M \geqslant 40\,M_\odot$ can be formed but do not eject any heavy elements via their supernova explosions.

It is shown by theoretical studies that the progenitors more massive than ~40–50 $M_\odot$ are more likely to collapse to form black holes without explosion (e.g., Fryer 1999; Heger & Woosley 2002). Chatzopoulos & Wheeler (2012) also predict that Pop III stars with mass as low as $M \sim 80\,M_\odot$ can explode as pair-instability supernovae rather than core-collapse supernovae, depending on the rotation of the progenitor star. The inferred scarcity of the chemical signature from $M \geqslant 40\,M_\odot$ is therefore consistent with these theoretical expectations.

Observational constraints on the masses of stellar mass black holes that are possible first-star remnants are helpful to distinguish between scenarios (1) and (2) (e.g., Özel et al. 2010; Abbott et al. 2016; Hartwig et al. 2016; Kinugawa et al. 2016), which are complementary to the chemical signature of EMP stars. For example, in the case of the scenario (1), the black hole mass distribution of the first stars should be the same as the compact remnant mass distribution obtained by Equation (1) in this work. Figure 14 shows the distribution of the masses of the compact remnant for the best-fit models (left) and that obtained by weighting with the p-values (right). The distribution is predominantly peaked at ~1.5–3 $M_\odot$, with a tail extending to ~46 $M_\odot$. In scenario (2), on the other hand, masses of the compact remnant could be much larger than those shown in Figure 14. Because mass loss is expected to be negligible for Pop III stars, due to the low opacity in their atmosphere preventing strong stellar winds, the final mass of the Pop III is likely to preserve its original mass, which may finally collapse without ejecting synthesized elements.

In scenario (3), the elements synthesized by Pop III stars in the range 40–100 $M_\odot$ are ejected to the inter-galactic medium, but low-mass stars do not form out of gas containing the ejecta, which may not satisfy various physical conditions required for low-mass star formation (e.g., Smith et al. 2015). The ejected elements would have contributed to the inter-galactic medium, and thus the elemental abundance signature of the >40 $M_\odot$ Pop III stars would remain in gas-phase metals in high-redshift objects. Measurements of gas-phase metallicity for high-redshift objects, such as Damped Lyα systems, would be useful to test this scenario (Kobayashi et al. 2011b; Cooke et al. 2017).

5.2. Explosion Energies

Another important finding of our analysis is for the explosion energies of the Pop III core-collapse supernovae; almost half of the sample stars are best-fitted with the model for a Pop III star with $M = 25\,M_\odot$, which explodes with high explosion energy ($E_{51} = 10$). Such a large fraction of hypernovae might be responsible for the chemical evolution of the Milky Way, not only in the solar neighborhood (e.g., Kobayashi et al. 2006; Romano et al. 2010; Kobayashi & Nakasato 2011), but also in the Galactic bulge (Howes et al. 2015). At low metallicity, [Zn/Fe] ratios show an increasing trend toward lower metallicities (Primas et al. 2000; Cayrel et al. 2004), which can be reproduced with hypernovae (Umeda & Nomoto 2005).

In the nearby universe, the most likely progenitors of hypernovae are thought to be rapidly rotating He cores that have stripped their H envelope and ended up as energetic Type Ibc supernovae; they are rare, compared to typical Type II SNe (e.g., Podsiadlowski et al. 2004). The rotational properties of the present-day and Pop III supernova progenitors should be very different because of the lack of mass loss due to the low opacity, which prevents the star from losing angular momentum. However, note that it is still debated whether the Pop III stars can maintain such high rotational velocity in the presence of magnetic fields (e.g., Yoon et al. 2012; Latif & Schleicher 2016).

At this moment, the only observational signatures of hypernovae among Pop III stars come from EMP stars, and there is no complementary observational evidence to support such a high fraction of hypernovae in the early universe. The direct detection of light curves of Pop III SNe (e.g., Smidt et al. 2014; Tolstov et al. 2016) is necessary to obtain more robust insights into the nature and the explosion mechanisms of the Pop III stars, which would eventually better constrain the Pop III IMF. That would require the detection of bright supernovae at high redshifts by next-generation instruments such as the Wide-Field Infrared Survey Telescope (WFIRST),

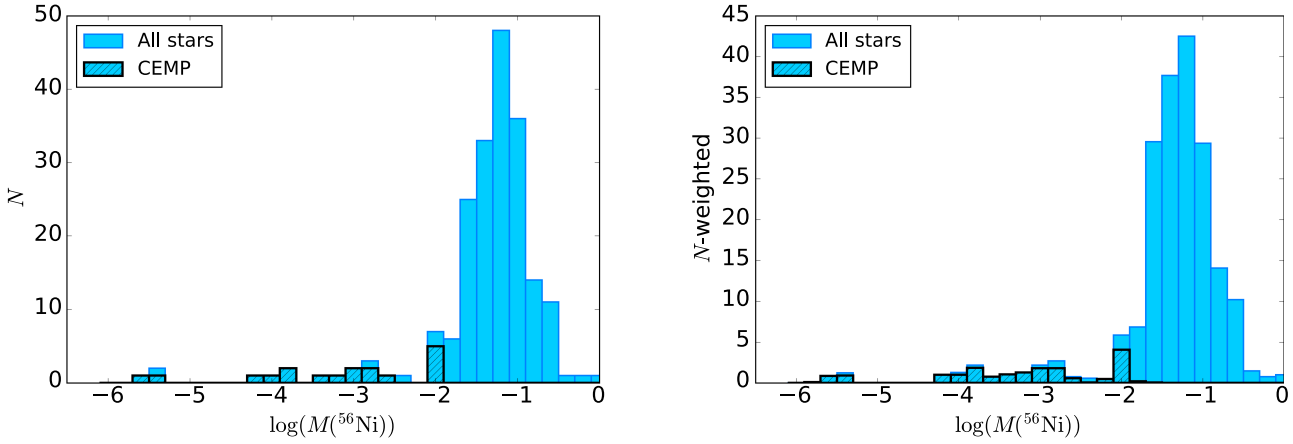

Figure 15. Similar histograms as in Figure 14, but for the ejected mass of ^{56}Ni.

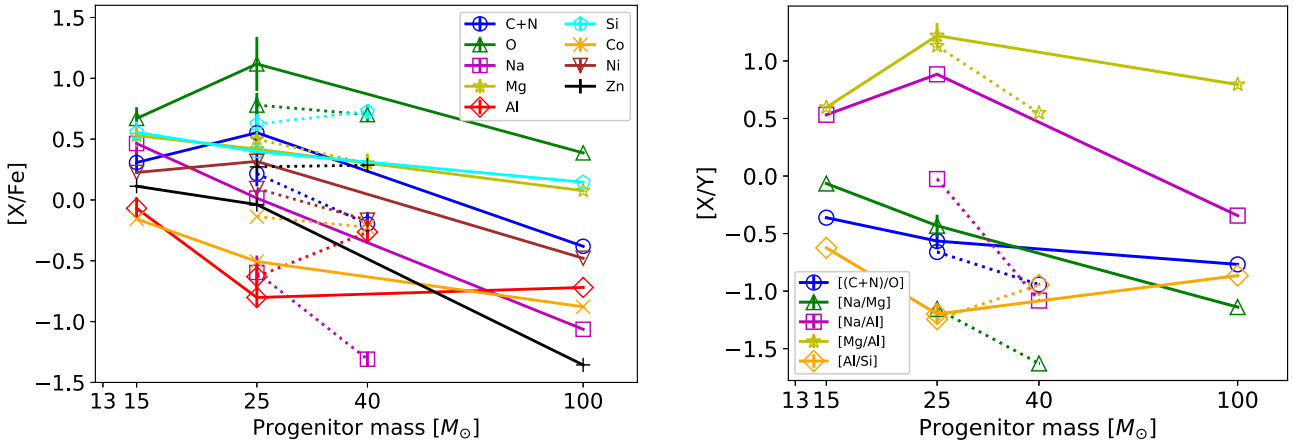

Figure 16. Abundance ratios as a function of masses of the Pop III stars for the best-fit models. The points correspond to a median [X/Fe] ratio among the best-fit models with $\chi^2 < 3$ for each of the 15SN, 25SN, 25HN, 40HN, and 100SN model. The error bars represent a median absolute deviation of the mean values. The points connected by the solid lines are for the normal-explosion-energy ($E_{51} = 1$) model, while the points connected by the dotted lines are for the hypernova ($E_{51} > 1$) models. The left panel is for the ratios relative to Fe and the right panel shows the ratios among C+N, O, Na, Mg, Al, and Si, for which abundance ratios are less affected by the choice of the mixing-fallback parameters.

the Large Synoptic Survey Telescope (LSST), or the *James Webb Space Telescope* (*JWST*; Hartwig et al. 2017).

5.3. Ejected Mass of ^{56}Ni

The yield of radioactive ^{56}Ni is one of the main sources of luminosity in supernovae. The ejected ^{56}Ni mass is measured by multi-color light-curve analyses of local supernovae. Also, this isotope finally decays to ^{56}Fe, the primary stable isotope of Fe. Figure 15 shows a histogram of ejected mass of the ^{56}Ni from the best-fit models. It can be seen from both the direct count of the best-fit models (left) and the χ^2_ν-weighted count that the ejected ^{56}Ni mass is predominantly 0.01–0.1 $M_\odot$. These masses are similar to those estimated by light-curve analysis of local supernova observations (e.g., Müller et al. 2017). On the other hand, the low-^{56}Ni mass tail is very different from the distribution of the rest of the sample, as the tail is caused from the existence of CEMP stars. The fraction of objects that are best-fitted with models that eject only small amount of $M(^{56}\mathrm{Ni}) < 0.01\,M_\odot$, which presumably corresponds to faint supernovae, is ∼10% of the first supernovae. Whether or not the typical ejected ^{56}Ni masses and the fraction of faint supernovae implied by the present analysis is consistent with the amount of metals in present-day galaxies should be tested through chemical evolution models with our yield of faint supernovae ($<10^{-3}\,M_\odot$).

5.4. Element Ratios as the Mass Indicator

Through our analysis, we can also propose the mass indicator of element ratios. In the previous sections, we obtained the best-fit model parameters to each EMP star. Based on these best-fit models, we investigate which abundance ratios best correlate with progenitor masses.

Figure 16 shows the median abundance ratios of the best-fit models (15SN, 25SN, 25HN, 40HN, and 100SN models) plotted against the progenitor masses (i.e., either 15, 25, 40, or 100 $M_\odot$). The left and right panels show abundance ratios relative to Fe and the ratios among the light elements, respectively. The solid and dotted lines indicate the trends for the supernova (15SN/25SN/100SN) models and the hypernova (25HN/40HN) models, respectively. The error bars in these plots represent the median absolute deviation of the best-fit models of a given progenitor mass/explosion energy.

As can be seen in the left panel, the [Na/Fe], [Mg/Fe], [Si/Fe], [Co/Fe], and [Zn/Fe] ratios monotonically decrease with the progenitor mass for the SN models (solid lines). These ratios, however, do not necessarily correlate with the mass for the HN models (dotted lines). This result highlights the importance of constraining the explosion energies from multiple abundance measurements including, e.g., a [Zn/Fe] ratio.

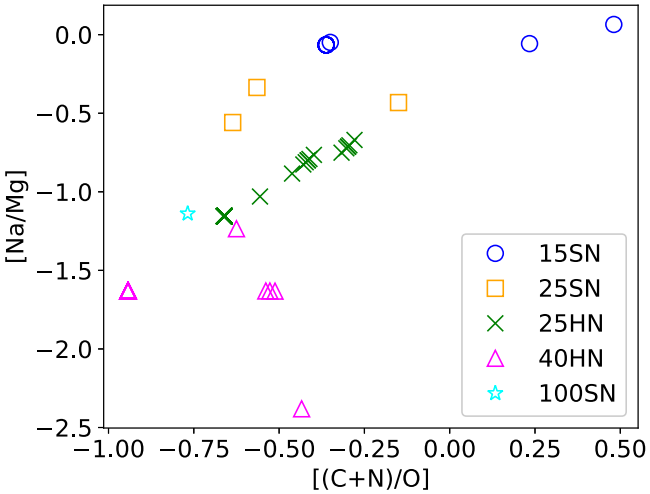

Figure 17. [(C+N)/O] vs. [Na/Mg] ratios for the best-fit models with $\chi^2 < 3$.

Among the light elements, shown in the right panel, [(C+N)/O] and [Na/Mg] ratios have negative correlation with progenitor masses for both the SN and HN models. The trend for the [(C+N)/O] ratio to decrease with increases in the Pop III main-sequence masses stems from the fact that C is mainly synthesized in the C+O layer between the He layer and the convective O core, the temperature of which is moderately high, ignites the He burning but not the C burning. Because production of O more strongly depends on temperature, and hence main-sequence masses, the C mass increases more slowly than the O mass with the main-sequence masses. The trend of [Na/Mg] resulted from the fact that synthesis of Na is less efficient in the C shell burning with higher temperature, which is typically realized for more massive Pop III stars.

To summarize, among the best-fit models considered in this work, the elements that are sensitive to the progenitor masses are the ratios between C+N, O, Na, and Mg. Figure 17 summarizes the locations in the [(C+N)/O] versus [Na/Mg] ratios for the best-fit models. The figure shows that a star with [Na/Mg] > -1.0 and [(C+N)/O] > -0.6 is more likely to be fitted with either the 15SN, 25SN, or 25HN models, while a star with [Na/Mg] < -1.0 and with [(C+N)/O] < -0.4 is more likely to be fitted with either the 40HN or 100SN models.

The correlation of the C/O ratio with the progenitor masses is expected from stellar evolution theories. The ratio in supernova ejecta, however, could significantly depend on the mixing-fallback process. At the same time, Na is burnt to Mg and Al in explosive nucleosynthesis, and thus the Na/Mg ratio depends on not only Pop III mass but also the explosion energies. Therefore, we emphasize that multiple elemental abundance measurements, other than the [(C+N)/O] and [Na/Mg] ratios, are also essential to resolve the degeneracy among the mixing-fallback process, the explosion energies, and the masses of the Pop III supernovae.

5.5. Limitations of the Present Approach

5.5.1. Uncertainties in Stellar Evolution

One of the major limitations of this study is that the Pop III model employed does not include the effect of stellar rotation. Rotation has been suggested to play an important role in determining the structure and nucleosynthetic yields of massive stars (Maeder & Meynet 2001; Hirschi 2007; Joggerst et al. 2010b). In a rotating Pop III stellar evolution model, production of ^{14}N is enhanced as the result of ^{12}C mixed from the helium-burning shell into the hydrogen-burning shell, in which the CNO cycle takes place (Meynet & Maeder 2002). Consequently, intermediate-mass isotopes such as ^{23}Na or ^{27}Al are also produced through a series of alpha capture reactions on ^{14}N (Takahashi et al. 2014). Therefore, the abundance ratios involving Na or Al may not clearly correlate with the Pop III progenitor mass if the star had rotation.

Predictions regarding these odd-Z elements are also affected by the treatment of overshooting or the uncertainty in the ^{12}C(α, γ)^{16}O reaction rate (Chieffi & Limongi 2002). Therefore, the predictions regarding Na and Al, in particular, as a Pop III mass indicator should be viewed with caution.

5.5.2. Explosive Nucleosynthesis in Multi-dimensional Simulation

In this work, we utilize the mixing-fallback model applied to the one-dimensional nucleosynthesis calculation in order to approximate the Pop III yields of aspherical supernovae. An important issue to be verified is the departure of the calculated yields from those predicted by multi-dimensional simulations of aspherical supernovae.

Tominaga (2009) performed a two-dimensional hydrodynamical and nucleosynthesis calculation for an aspherical jet-induced explosion of a 40 $M_\odot$ Pop III star. The results suggest that the angle-averaged yields for many elements are in agreement with those from the particular parameterization in the mixing-fallback model applied to the one-dimensional nucleosynthesis calculation. However, elemental ratios such as [Sc, Ti, V, Cr, Co, Zn/Fe] are enhanced in the simulation, as a result of the high-entropy environment realized only in the two-dimensional calculation of the jet-induced supernovae. It is also demonstrated that the predicted yields largely depend on the angle from the jet axis; thus, if the ejecta is not well-mixed, the elemental abundances imprinted on the next generation of stars could be significantly different from those predicted by the mixing-fallback model (Tominaga 2009).

In order to better constrain the Pop III progenitor of EMP stars based on the measurements of Sc, Ti, V, Cr, Co, and Zn abundances, multi-dimensional simulations with various progenitor masses and explosion energies are needed.

6. Conclusion

We calculate supernova yields of Pop III stars in the mass range 13–100 $M_\odot$ for low ($E_{51} < 1$), normal ($E_{51} = 1$), and high ($E_{51} > 1$) explosion energies that best reproduce elemental abundance measurements of ∼200 EMP stars taken from recent literature in the framework of the mixing-fallback model. The results can be summarized as follows.

1. The observed abundances of the majority of the present sample of EMP stars are best-reproduced with the Pop III yields from progenitors less massive than 40 $M_\odot$. Almost half of the sample stars are best-fitted with the model for a Pop III star with $M = 25\,M_\odot$, which explodes with high explosion energy ($E_{51} = 10$).
2. The predominance of the $M < 40\,M_\odot$ best-fit Pop III models is affected by the fiducial observational errors we have assigned to the data (0.1–0.3 dex). Obtaining a tighter constraint on the Pop III masses requires the errors to be smaller than the fiducial values.
3. We have also examined the effects of the two major systematic uncertainties: (1) NLTE effects on Al abundances

and (2) the effect of non-measurements for specific elements. For (1), the uniform NLTE correction for the Al abundance by 0.6 dex results in a change in the best-fit models from $M = 25\,M_{\odot}$ to $M \leqslant 15\,M_{\odot}$ for some of our sample stars, which highlights the necessity of the NLTE abundance measurements to discriminate between these progenitor masses. For (2), the lack of either the Si or Zn measurements leads to the change in the best-fit Pop III models, and thus measurement of these elements is particularly important. In both (1) and (2), the main results, remain unchanged, i.e., the Pop III mass distribution is still peaked at $M = 25\,M_{\odot}$ and the dominant contribution still comes from $M < 40\,M_{\odot}$.

4. The mixing-fallback parameters for most of the EMP stars are characterized by (1)$M_{\rm mix}$ smaller than the mass below which the explosive nucleosynthesis take place and (2) $f_{\rm ej} \sim 0.01$–0.5. The results indicate that the progenitor Pop III super-/hypernovae have predominantly left behind compact remnants with masses less than $<5\,M_{\odot}$ and ejected $\sim$0.01–0.1 $M_{\odot}$ of ^{56}Ni.
5. The CEMP stars ([(C+N)/Fe] > 1.0) in our sample are best-fitted with Pop III models that have progenitor masses similar to those that fit the other C-normal EMP stars. On the other hand, the best-fit mixing-fallback parameters for the CEMP stars are largely different from those of the majority of other EMP stars, in that the CEMP are explained by the large mixing region and the small ejected fraction. The CEMP stars with Mg enhancement ([Mg/Fe] > 1) are explained by the model for a Pop III star with $M = 25\,M_{\odot}$ exploding with high explosion energy (hypernova).
6. The resulting mass distribution of the progenitor Pop III of the EMP stars decreases at $M < 25\,M_{\odot}$, which is not consistent with the Salpeter IMF. The drop at $M \geqslant 40_{\odot}$ suggests either that (1) the formation of the first stars with $M \geqslant 40\,M_{\odot}$ is suppressed, that (2) the $M \geqslant 40\,M_{\odot}$ first stars tend to directly collapse into black holes without ejecting any heavy elements to be incorporated into the next generation of low-mass stars, or that (3) the supernovae of higher-mass Pop III stars inhibit the formation of the next generation of low-mass stars. These scenarios predict different distributions of mass for the compact remnants and ejected mass of ^{56}Ni, and thus should be tested with other observational probes, such as the masses of the stellar-mass black holes and light curves of Pop III supernovae, in future observations.
7. Based on the best-fit models, we propose diagnostic abundance ratios sensitive to the Pop III progenitor masses, where the [(C+N)/O] ratios best correlate with the progenitor masses. The Na, Mg, and Al abundances could also be sensitive to the progenitor masses if the progenitor stellar rotation does not significantly affect the abundances of these elements.

These results demonstrate that the elemental abundances in EMP stars have useful implications on the physical properties of the Pop III stars and their supernova explosions. Ongoing and future photometric and spectroscopic surveys, such as the SDSS/APOGEE (Majewski et al. 2017), GALAH (De Silva et al. 2015), Pristine (Starkenburg et al. 2017), LAMOST (Zhao et al. 2012), and their follow-up observations (e.g., Li et al. 2015) to accurately measure most of the important key elements for large samples of EMP stars are crucial to obtain more robust insights into the nature of the Pop III stars.

The present analysis method, however, is based on various assumptions regarding the progenitor Pop III stellar evolution (rotation) and supernova explosions, which should be verified with more realistic multi-dimensional nucleosynthesis calculations. At the same time, the present results highlight the importance of complementary high-redshift supernova observations with next-generation photometric and spectroscopic facilities (e.g., *WFIRST*, *LSST*, and *JWST*; see Hartwig et al. 2017) to connect the nucleosynthetic signatures of EMP stars with the initial mass function of the Pop III stars.

M.N.I. thanks A. Tolstov, S.-C. Leung, A. Zhiglo, and T. Hartwig for fruitful conversations on theoretical aspects of supernovae, nucleosynthesis and/or cosmological simulations. The authors are grateful to N. Christlieb, A. Frebel, and M. Limongi for helpful comments and suggestions. C.K. thanks Marii Shirouzu and Natsuko Izutani for the earlier attempts on this topic. This work has been supported by the World Premier International Research Center Initiative (WPI Initiative), MEXT, Japan, and JSPS KAKENHI Grant Numbers JP26400222, JP16H02168, JP17K05382, JP17K14249, and the Endowed Research Unit "Dark side of the Universe" by Hamamatsu Photonics KK at Kavli IPMU.

Appendix
Table of Best-fit Models

Table 3 presents [X/H] abundances of the best-fit models and the observational data from literature used in the abundance fitting.

Table 3
Best-fit Models and Observed Abundances from Literature

Starname	M	E	$M_{\rm mix}$	Log$f_{\rm ej}$	[C/H]$_{\rm mod}$	Flag[a]	[N/H]$_{\rm mod}$	⋯	[C/H]$_{\rm obs}$	Flag[a]	[N/H]$_{\rm obs}$	⋯	Ref.[b]
HE0020-1741	13	0.5	1.7	−1.1	−3.49	1	−4.57	⋯	−2.24	1	⋯	⋯	9

Notes.
[a] Flags for the abundances: 1 for used value, −1 for upper limit, −2 for lower limit.
[b] List of References: (1) Yong et al. (2013a), (2) Cohen et al. (2013), (3) Roederer et al. (2014), (4) Jacobson et al. (2015), (5) Hansen et al. (2014), (6) Placco et al. (2015), (7) Frebel et al. (2015), (8) Meléndez et al. (2016), (9) Placco et al. (2016).

(This table is available in its entirety in machine-readable form.)

ORCID iDs

Miho N. Ishigaki https://orcid.org/0000-0003-4656-0241
Nozomu Tominaga https://orcid.org/0000-0001-8537-3153
Chiaki Kobayashi https://orcid.org/0000-0002-4343-0487
Ken'ichi Nomoto https://orcid.org/0000-0001-9553-0685

References

Abbott, B. P., Abbott, R., Abbott, T. D., et al. 2016, PhRvL, 116, 061102
Aoki, W., Beers, T. C., Lee, Y. S., et al. 2013, AJ, 145, 13
Aoki, W., Frebel, A., Christlieb, N., et al. 2006, ApJ, 639, 897
Aoki, W., Tominaga, N., Beers, T. C., Honda, S., & Lee, Y. S. 2014, Sci, 345, 912
Asplund, M., Grevesse, N., Sauval, A. J., & Scott, P. 2009, ARA&A, 47, 481
Audouze, J., & Silk, J. 1995, ApJL, 451, L49
Baumueller, D., & Gehren, T. 1997, A&A, 325, 1088
Beers, T. C., & Christlieb, N. 2005, ARA&A, 43, 531
Bergemann, M., Pickering, J. C., & Gehren, T. 2010, MNRAS, 401, 1334
Bessell, M. S., Collet, R., Keller, S. C., et al. 2015, ApJL, 806, L16
Bromm, V., & Larson, R. B. 2004, ARA&A, 42, 79
Bromm, V., & Loeb, A. 2003, Natur, 425, 812
Bromm, V., & Yoshida, N. 2011, ARA&A, 49, 373
Burrows, A. 2013, RvMP, 85, 245
Caughlan, G. R., & Fowler, W. A. 1988, ADNDT, 40, 283
Cayrel, R., Depagne, E., Spite, M., et al. 2004, A&A, 416, 1117
Cen, R., & Riquelme, M. A. 2008, ApJ, 674, 644
Chatzopoulos, E., & Wheeler, J. C. 2012, ApJ, 748, 42
Chen, K.-J., Heger, A., Whalen, D. J., et al. 2017a, MNRAS, 467, 4731
Chen, K.-J., Whalen, D. J., Wollenberg, K. M. J., Glover, S. C. O., & Klessen, R. S. 2017b, ApJ, 844, 111
Chieffi, A., & Limongi, M. 2002, ApJ, 577, 281
Christlieb, N., Bessell, M. S., Beers, T. C., et al. 2002, Natur, 419, 904
Clark, P. C., Glover, S. C. O., Klessen, R. S., & Bromm, V. 2011, ApJ, 727, 110
Cohen, J. G., Christlieb, N., Thompson, I., et al. 2013, ApJ, 778, 56
Cohen, J. G., McWilliam, A., Christlieb, N., et al. 2007, ApJL, 659, L161
Collet, R., Asplund, M., & Trampedach, R. 2006, ApJL, 644, L121
Cooke, R. J., & Madau, P. 2014, ApJ, 791, 116
Cooke, R. J., Pettini, M., & Steidel, C. C. 2017, MNRAS, 467, 802
De Silva, G. M., Freeman, K. C., Bland-Hawthorn, J., et al. 2015, MNRAS, 449, 2604
Fabbian, D., Asplund, M., Barklem, P. S., Carlsson, M., & Kiselman, D. 2009, A&A, 500, 1221
Fowler, W. A. 1984, RvMP, 56, 149
Frebel, A., Aoki, W., Christlieb, N., et al. 2005, Natur, 434, 871
Frebel, A., Chiti, A., Ji, A. P., Jacobson, H. R., & Placco, V. M. 2015, ApJL, 810, L27
Frebel, A., Collet, R., Eriksson, K., Christlieb, N., & Aoki, W. 2008, ApJ, 684, 588
Frebel, A., & Norris, J. E. 2015, ARA&A, 53, 631
Fryer, C. L. 1999, ApJ, 522, 413
Gallagher, A. J., Caffau, E., Bonifacio, P., et al. 2016, A&A, 593, A48
Greif, T. H., Johnson, J. L., Bromm, V., & Klessen, R. S. 2007, ApJ, 670, 1
Greif, T. H., Springel, V., White, S. D. M., et al. 2011, ApJ, 737, 75
Hansen, T., Hansen, C. J., Christlieb, N., et al. 2014, ApJ, 787, 162
Hartwig, T., Bromm, V., Klessen, R. S., & Glover, S. C. O. 2015, MNRAS, 447, 3892
Hartwig, T., Bromm, V., & Loeb, A. 2017, MNRAS, submitted (arXiv:1711.05742)
Hartwig, T., Volonteri, M., Bromm, V., et al. 2016, MNRAS, 460, L74
Heger, A., & Woosley, S. E. 2002, ApJ, 567, 532
Heger, A., & Woosley, S. E. 2010, ApJ, 724, 341
Hirano, S., & Bromm, V. 2017, MNRAS, 470, 898
Hirano, S., Hosokawa, T., Yoshida, N., et al. 2014, ApJ, 781, 60
Hirschi, R. 2007, A&A, 461, 571
Hix, W. R., & Thielemann, F.-K. 1996, ApJ, 460, 869
Hosokawa, T., Hirano, S., Kuiper, R., et al. 2016, ApJ, 824, 119
Hosokawa, T., Omukai, K., Yoshida, N., & Yorke, H. W. 2011, Sci, 334, 1250
Howes, L. M., Casey, A. R., Asplund, M., et al. 2015, Natur, 527, 484
Ishigaki, M. N., Tominaga, N., Kobayashi, C., & Nomoto, K. 2014, ApJL, 792, L32
Ishiyama, T., Sudo, K., Yokoi, S., et al. 2016, ApJ, 826, 9
Iwamoto, N., Umeda, H., Tominaga, N., Nomoto, K., & Maeda, K. 2005, Sci, 309, 451
Jacobson, H. R., Keller, S., Frebel, A., et al. 2015, ApJ, 807, 171
Janka, H.-T. 2012, ARNPS, 62, 407
Joggerst, C. C., Almgren, A., Bell, J., et al. 2010a, ApJ, 709, 11
Joggerst, C. C., Almgren, A., & Woosley, S. E. 2010b, ApJ, 723, 353
Joggerst, C. C., Woosley, S. E., & Heger, A. 2009, ApJ, 693, 1780
Karlsson, T., Bromm, V., & Bland-Hawthorn, J. 2013, RvMP, 85, 809
Karlsson, T., Johnson, J. L., & Bromm, V. 2008, ApJ, 679, 6
Keller, S. C., Bessell, M. S., Frebel, A., et al. 2014, Natur, 506, 463
Kinugawa, T., Miyamoto, A., Kanda, N., & Nakamura, T. 2016, MNRAS, 456, 1093
Kitayama, T., & Yoshida, N. 2005, ApJ, 630, 675
Kitayama, T., Yoshida, N., Susa, H., & Umemura, M. 2004, ApJ, 613, 631
Kobayashi, C., Ishigaki, M. N., Tominaga, N., & Nomoto, K. 2014, ApJL, 785, L5
Kobayashi, C., Izutani, N., Karakas, A. I., et al. 2011a, ApJL, 739, L57
Kobayashi, C., & Nakasato, N. 2011, ApJ, 729, 16
Kobayashi, C., Tominaga, N., & Nomoto, K. 2011b, ApJL, 730, L14
Kobayashi, C., Umeda, H., Nomoto, K., Tominaga, N., & Ohkubo, T. 2006, ApJ, 653, 1145
Kotake, K., Sumiyoshi, K., Yamada, S., et al. 2012, PTEP, 2012, 01A301
Lai, D. K., Bolte, M., Johnson, J. A., et al. 2008, ApJ, 681, 1524
Latif, M. A., & Schleicher, D. R. G. 2016, A&A, 585, A151
Li, H., Aoki, W., Zhao, G., et al. 2015, PASJ, 67, 84
Limongi, M., Chieffi, A., & Bonifacio, P. 2003, ApJL, 594, L123
Lind, K., Asplund, M., Barklem, P. S., & Belyaev, A. K. 2011, A&A, 528, A103
Maeda, K., Kawabata, K., Mazzali, P. A., et al. 2008, Sci, 319, 1220
Maeder, A., & Meynet, G. 2001, A&A, 373, 555
Magg, M., Hartwig, T., Agarwal, B., et al. 2018, MNRAS, 473, 5308
Majewski, S. R., Schiavon, R. P., Frinchaboy, P. M., et al. 2017, AJ, 154, 94
Meléndez, J., Placco, V. M., Tucci-Maia, M., et al. 2016, A&A, 585, L5
Meynet, G., Ekström, S., & Maeder, A. 2006, A&A, 447, 623
Meynet, G., & Maeder, A. 2002, A&A, 381, L25
Müller, T., Prieto, J. L., Pejcha, O., & Clocchiatti, A. 2017, ApJ, 841, 127
Nomoto, K., & Hashimoto, M. 1988, PhR, 163, 13
Nomoto, K., Kobayashi, C., & Tominaga, N. 2013, ARA&A, 51, 457
Nomoto, K., Tominaga, N., Umeda, H., Kobayashi, C., & Maeda, K. 2006, NuPhA, 777, 424
Nordlander, T., Amarsi, A. M., Lind, K., et al. 2017, A&A, 597, A6
Ohkubo, T., Nomoto, K., Umeda, H., Yoshida, N., & Tsuruta, S. 2009, ApJ, 706, 1184
Ohkubo, T., Umeda, H., Maeda, K., et al. 2006, ApJ, 645, 1352
Omukai, K., Tsuribe, T., Schneider, R., & Ferrara, A. 2005, ApJ, 626, 627
Özel, F., Psaltis, D., Narayan, R., & McClintock, J. E. 2010, ApJ, 725, 1918
Placco, V. M., Frebel, A., Beers, T. C., et al. 2016, ApJ, 833, 21
Placco, V. M., Frebel, A., Beers, T. C., & Stancliffe, R. J. 2014, ApJ, 797, 21
Placco, V. M., Frebel, A., Lee, Y. S., et al. 2015, ApJ, 809, 136
Podsiadlowski, P., Mazzali, P. A., Nomoto, K., Lazzati, D., & Cappellaro, E. 2004, ApJL, 607, L17
Primas, F., Brugamyer, E., Sneden, C., et al. 2000, in Proc. The First Stars Workshop, ed. A. Weiss, T. G. Abel, & V. Hill (Garching: Springer), 51
Ritter, J. S., Safranek-Shrader, C., Gnat, O., Milosavljević, M., & Bromm, V. 2012, ApJ, 761, 56
Ritter, J. S., Safranek-Shrader, C., Milosavljević, M., & Bromm, V. 2016, MNRAS, 463, 3354
Roederer, I. U., Preston, G. W., Thompson, I. B., et al. 2014, AJ, 147, 136
Romano, D., Karakas, A. I., Tosi, M., & Matteucci, F. 2010, A&A, 522, A32
Sluder, A., Ritter, J. S., Safranek-Shrader, C., Milosavljević, M., & Bromm, V. 2016, MNRAS, 456, 1410
Smidt, J., Whalen, D. J., Wiggins, B. K., et al. 2014, ApJ, 797, 97
Smith, B. D., Wise, J. H., O'Shea, B. W., Norman, M. L., & Khochfar, S. 2015, MNRAS, 452, 2822
Sneden, C., Cowan, J. J., Kobayashi, C., et al. 2016, ApJ, 817, 53
Stacy, A., & Bromm, V. 2013, MNRAS, 433, 1094
Stacy, A., Bromm, V., & Lee, A. T. 2016, MNRAS, 462, 1307
Starkenburg, E., Martin, N., Youakim, K., et al. 2017, MNRAS, 471, 2587
Suda, T., Katsuta, Y., Yamada, S., et al. 2008, PASJ, 60, 1159
Susa, H. 2013, ApJ, 773, 185
Susa, H., Hasegawa, K., & Tominaga, N. 2014, ApJ, 792, 32
Takahashi, K., Umeda, H., & Yoshida, T. 2014, ApJ, 794, 40
Tolstov, A., Nomoto, K., Tominaga, N., et al. 2016, ApJ, 821, 124
Tominaga, N. 2009, ApJ, 690, 526
Tominaga, N., Iwamoto, N., & Nomoto, K. 2014, ApJ, 785, 98
Tominaga, N., Maeda, K., Umeda, H., et al. 2007a, ApJL, 657, L77
Tominaga, N., Umeda, H., & Nomoto, K. 2007b, ApJ, 660, 516
Tumlinson, J., Venkatesan, A., & Shull, J. M. 2004, ApJ, 612, 602

Umeda, H., & Nomoto, K. 2002, ApJ, 565, 385
Umeda, H., & Nomoto, K. 2003, Natur, 422, 871
Umeda, H., & Nomoto, K. 2005, ApJ, 619, 427
Umeda, H., Nomoto, K., & Nakamura, T. 2000, in Proc. The First Stars Workshop, ed. A. Weiss, T. G. Abel, & V. Hill (Garching: Springer), 150
Whalen, D., Abel, T., & Norman, M. L. 2004, ApJ, 610, 14
Whalen, D., van Veelen, B., O'Shea, B. W., & Norman, M. L. 2008, ApJ, 682, 49
Wongwathanarat, A., Müller, E., & Janka, H.-T. 2015, A&A, 577, A48
Yong, D., Norris, J. E., Bessell, M. S., et al. 2013a, ApJ, 762, 26
Yong, D., Norris, J. E., Bessell, M. S., et al. 2013b, ApJ, 762, 27
Yoon, S.-C., Dierks, A., & Langer, N. 2012, A&A, 542, A113
Zhang, W., Woosley, S. E., & Heger, A. 2008, ApJ, 679, 639
Zhao, G., Zhao, Y.-H., Chu, Y.-Q., Jing, Y.-P., & Deng, L.-C. 2012, RAA, 12, 723